Intelligent Reflecting Surface-Assisted NLOS Sensing With OFDM Signals

Jilin Wang , Graduate Student Member, IEEE, Jun Fang , Senior Member, IEEE, Hongbin Li , Fellow, IEEE, and Lei Huang , Senior Member, IEEE

Abstract-This work addresses the problem of intelligent reflecting surface (IRS) assisted target sensing in a non-line-ofsight (NLOS) scenario, where an IRS is employed to facilitate the radar/access point (AP) to sense the targets when the lineof-sight (LOS) path between the AP and the target is blocked by obstacles. To sense the targets, the AP transmits a train of uniformly-spaced orthogonal frequency division multiplexing (OFDM) pulses, and then perceives the targets based on the echoes from the AP-IRS-targets-IRS-AP channel. To resolve an inherent scaling ambiguity associated with IRS-assisted NLOS sensing, we propose a two-phase sensing scheme by exploiting the diversity in the illumination pattern of the IRS across two different phases. Specifically, the received echo signals from the two phases are formulated as third-order tensors. Then a canonical polyadic (CP) decomposition-based method is developed to estimate each target's parameters including the direction of arrival (DOA), Doppler shift and time delay. Our analysis reveals that the proposed method achieves reliable NLOS sensing using a modest quantity of pulse/subcarrier resources. Simulation results are provided to show the effectiveness of the proposed method under the challenging scenario where the degrees-of-freedom provided by the AP-IRS channel are not enough for resolving the scaling ambiguity.

Index Terms—Intelligent reflecting surface (IRS), NLOS wireless sensing, OFDM, canonical polyadic (CP) decomposition.

Received 20 May 2024; revised 11 September 2024 and 14 October 2024; accepted 11 November 2024. Date of publication 14 November 2024; date of current version 27 November 2024. This work was supported in part by the National Science Foundation of China under Grant 62471106. The work of Hongbin Li was supported in part by the National Science Foundation under Grant ECCS-1923739, Grant ECCS-2212940, Grant ECCS-2332534, and Grant CCF-2316865. An earlier version of this paper was presented in part at EUSIPCO 2024. The current work is a full version which includes theoretical analyses and provides a more detailed algorithmic development. The associate editor coordinating the review of this article and approving it for publication was Prof. Rodrigo C. de Lamare. (Corresponding authors: Jun Fang; Lei Huang.)

Jilin Wang and Jun Fang are with the National Key Laboratory of Wireless Communications, University of Electronic Science and Technology of China, Chengdu 611731, China (e-mail: jilinwang@std.uestc.edu.cn; JunFang@uestc.edu.cn).

Hongbin Li is with the Department of Electrical and Computer Engineering, Stevens Institute of Technology, Hoboken, NJ 07030 USA (e-mail: Hongbin. Li@stevens.edu).

Lei Huang is with the State Key Laboratory of Radio Frequency Heterogeneous Integration, Shenzhen University, Shenzhen 518060, China (e-mail: lhuang@szu.edu.cn).

Digital Object Identifier 10.1109/TSP.2024.3498861

I. INTRODUCTION

A. Background

NTELLIGENT reflecting surface (IRS) has received a great amount of attention in wireless communications due to its ability of reconfiguring wireless propagation channels [1], [2], [3]. Specifically, IRS is made of a newly developed metamaterial comprising a large number of reconfigurable passive components. Through a smart controller, the phase and amplitude of each unit on the IRS can be flexibly adjusted. By properly designing the reflection coefficients, the propagation environment can be customized to enhance/diminish signals of interest. This allows for coherent or destructive addition of reflected signals at the receiver, enabling passive beamforming, increased spectral efficiency, interference suppression, and other benefits [4], [5], [6], [7]. In recent years, the integration of wireless sensing as a new functionality into future sixth-generation (6G) wireless networks has attracted increasing research attention [8], [9], [10], [11]. Wireless sensing typically involves extracting target information, such as the angle and distance, through the lineof-sight (LOS) path between the target and the wireless node. However, in some urban scenarios, the targets of interest may be distributed in the non-line-of-sight (NLOS) region of the wireless node, rendering LOS path-based target sensing ineffective. To address this challenge, IRS was introduced as an energyefficient and cost-effective anchor node with known locations, creating a virtual LOS link between the sensing node and the target to enhance performance [12], [13], [14], [15], [16], [17], [18], [19], [20], [21], [22], [23], [24], [25].

B. Related Works

There have been some prior works investigating IRS-enabled wireless sensing (i.e., NLOS detection/estimation) [12], [13], [14], [15], [16], [17], [18], [19], [20], [21], [22] and IRS-assisted integrated sensing and communication (ISAC) systems [23], [24], [25]. For the IRS-aided NLOS detection problem, the work [12] developed a radar equation for the IRS-aided NLOS scenario, and evaluated the sensing performance in terms of signal-to-noise ratio (SNR) and signal-to-clutter ratio (SCR). In [13], [14], [15], an IRS-aided multi-input multi-output (MIMO) radar detection problem was considered, in which the IRS is placed in the vicinity of radar transmitter (or receiver) to help illuminate (observe) prospective targets. A generalized likelihood ratio test (GLRT) detector was derived and the IRS phase shifts

1053-587X © 2024 IEEE. Personal use is permitted, but republication/redistribution requires IEEE permission. See https://www.ieee.org/publications/rights/index.html for more information.

were optimized to maximize the probability of detection given a fixed false alarm probability. An IRS-assisted radar system for target surveillance in a cluttered environment was studied in [16], where the active beamformer at the radar transmitter and the passive phase-shift matrices at IRSs are jointly optimized to maximize the minimum target illumination power at multiple target locations. The moving target detection problem in a multi-IRS-aided OFDM radar system was considered in [17], where the authors derived a bi-quadratic program which jointly designs the OFDM signal and IRS phase shifts to optimize the target detection performance.

In addition to detection, the estimation problem was studied for IRS-aided NLOS sensing systems. The work [18] considered an IRS-self-sensing architecture, where an IRS controller is employed to transmit probing signals, and dedicated sensors are installed at the IRS for location/angle estimation based on the echo signals via the BS-IRS-target-IRS sensor link and the BS-target-IRS sensor link. An IRS-enabled pulse-Doppler radar system was considered in [19], where the minimum variance for the best linear unbiased estimator (BLUE) of the target back-scattering coefficient is derived, and then the IRS phase shifts were optimized by minimizing the mean squared error of estimated target parameter. In [20], a multi-IRS assisted sensing system was introduced, where the IRS forms a passive directional beam to scan the space to locate the potential target that is beyond the sight of the AP. Following [20], the work [21] explored semi-passive IRS-based sensing as a means to mitigate the high signal attenuation issue inherent in passive IRS sensing systems. Moreover, the work [22] examined the estimation of the DOA in an IRS-enabled NLOS sensing system, where the transmit beamformer at the AP and the passive beamformer at the IRS were jointly optimized by minimizing the Cramér-Rao bound (CRB). It is noted in [22] that an inherent scaling ambiguity exists in IRS-assisted NLOS sensing when the rank of the AP-IRS channel matrix is equal to one. This is because at least two degrees-of-freedom (DoFs) are required to identify both the complex path gain and the angular parameter of the target, otherwise the scaling ambiguity arises [26]. To resolve the inherent scaling ambiguity, the work [22] needs that the AP-IRS channel matrix contains at least two prominent singular values. Such a requirement, however, may not be satisfied in practice. Specifically, for IRS-assisted sensing, in order to compensate for the path loss caused by multiple reflections, the IRS is usually located within the sight of the AP and the AP-IRS channel is dominated by the LOS path, in which case the work [22] will experience a substantial amount of performance degradation. For this reason, it holds practical significance to study the scenario where the AP-IRS channel is dominated by the LOS path.

C. Our Contributions

In this paper, we consider the problem of target parameter estimation via an IRS-assisted sensing system. The AP transmits a train of uniformly-spaced OFDM pulses, and then perceives the targets based on the echo signal from the AP-IRS-targets-IRS-AP channel. To resolve the scaling ambiguity inherent in

IRS-assisted sensing, we, in this paper, propose a two-phase sensing method, where the entire sensing cycle consists of two phases, and each phase is assigned an individual IRS-phase-shift profile. By utilizing the diversity of the IRS illumination pattern across two phases, the received OFDM signals in two phases are represented by two third-order tensors, and a CP decomposition-based method is developed to uniquely identify the DOAs, time delays, and Doppler shifts of the targets even when there is only a single dominant path between the AP and the IRS. Additionally, a theoretical analysis is presented to provide a performance bound for the proposed sensing system. Simulation results demonstrate that the proposed method achieves an estimation accuracy that is close to the CRB, thereby validating the effectiveness of the proposed method.

In addition to the ability of resolving the inherent scaling ambiguity, our work presents some other advantages over [22]. First of all, the work [22] only studied the problem of DOA estimation, whereas our proposed method can identify not only the DOA, but also the distance and the Doppler shift parameters of the targets. Secondly, the work [22] considered only a single target scenario, and it is difficult to extend the proposed maximum likelihood estimator (MLE) to multi-target scenarios. As a comparison, our proposed method can handle multiple targets simultaneously.

The remainder of this paper is organized as follows. Section II introduces the system model as well as the signal model of the proposed IRS-assisted NLOS sensing system. Section III develops a two-phase sensing scheme, based on which the CP formulation, uniqueness conditions and CP decomposition are discussed. Section IV discuss how to estimate the target parameters from the estimated factor matrices. Section V presents the CRB analysis for the considered estimation problem. Simulation results are presented in Section VI, followed by concluding remarks in Section VII.

Notations: In this paper, scalars, column vectors, matrices and tensors are denoted by italic, lowercase boldface, uppercase boldface and calligraphic boldface letters, respectively. The symbols $(\cdot)^*$, $(\cdot)^T$, $(\cdot)^H$, $(\cdot)^{-1}$, $(\cdot)^{\dagger}$ denote the conjugate, transpose, conjugate transpose, inverse and pseudo-inverse, respectively. $\|\cdot\|_2$ and $\|\cdot\|_F$ denote the 2-norm and Frobenius norm, respectively. diag(a) denotes a diagonal matrix whose main diagonal elements are the elements of a. I_M denotes the identity matrix of size M. $[a]_i$, $[A]_{i,l}$, $[A]_{i,:}$, $[A]_{:,l}$ denote the ith element of a, the (i, l)th element of A, the ith row of A and the lth column of A, respectively. rank(A) and k_A denote the rank and Kruskal-rank of A, respectively. \otimes , \odot , \otimes and o denote the Kronecker, Khatri-Rao, Hadamard and outer products, respectively. j denotes the imaginary unit. $\Re\{\cdot\}$ and $\Im\{\cdot\}$ denote the real and imaginary parts of a complex number, respectively.

II. PROBLEM FORMULATION

A. System Model

Consider an IRS-assisted wireless sensing (i.e., radar) system, where the LOS path between the radar/access point and the target is blocked by obstacles (see Fig. 1). The access point (AP)

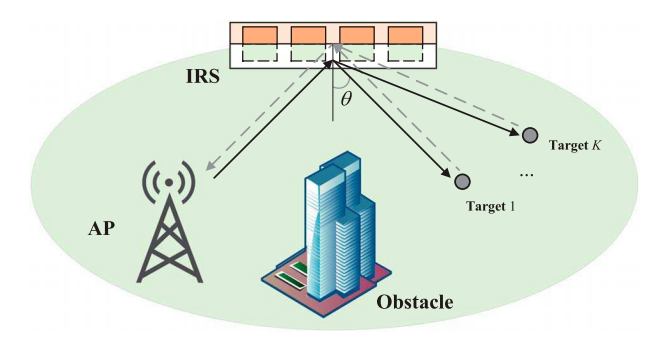


Fig. 1. Illustration of the considered IRS-assisted wireless communication system.

transmits a sensing signal and then perceives the targets based on the echo signal propagating through the AP-IRS-targets-IRS-AP channel. Suppose the AP is equipped with a uniform linear array (ULA) of M antennas, and the IRS is equipped with a ULA of N reflecting elements. Note that to facilitate the exposition of our proposed method, we consider the ULA configuration at the IRS. The proposed method can also be extended to planar array scenarios.

We assume that there are K targets located in the area that are illuminated by the IRS. Let $\boldsymbol{x}(t) \in \mathbb{C}^M$ denote the transmitted signal, and $\boldsymbol{G} \in \mathbb{C}^{N \times M}$ denote the channel matrix from the AP to the IRS. Since the locations of the AP and the IRS are predetermined, we assume that the channel matrix \boldsymbol{G} is known a priori. Each reflecting element of the IRS can independently reflect the incident signal with a reconfigurable phase shift. Define $\vartheta_n \in [0,2\pi]$ as the phase shift associated with the nth reflecting element of the IRS. Also, define the phase shift matrix of the IRS as

$$\mathbf{\Phi} = \operatorname{diag}(e^{j\vartheta_1}, \dots, e^{j\vartheta_n}) \in \mathbb{C}^{N \times N} \tag{1}$$

Let θ denote a target's DOA with respect to the IRS. The corresponding steering vector at the IRS can be written as

$$\boldsymbol{a}(\theta) = \frac{1}{\sqrt{N}} \left[1 \ e^{j2\pi \frac{d\sin(\theta)}{\lambda}} \ \cdots \ e^{j2\pi \frac{(N-1)d\sin(\theta)}{\lambda}} \right]^T \tag{2}$$

where d denotes the spacing between adjacent reflection elements, and λ is the wavelength of the carrier signal. For the kth target, the cascaded IRS-target-IRS channel can be written as

$$\boldsymbol{H}_k = \tilde{\alpha}_k \boldsymbol{a}(\theta_k) \boldsymbol{a}^T(\theta_k) \tag{3}$$

where $\tilde{\alpha}_k \in \mathbb{C}$ is used to characterize the round-trip path loss as well as the radar cross section (RCS) coefficient of the kth target. Define $\boldsymbol{H} \triangleq \sum_{k=1}^K \boldsymbol{H}_k$. In this paper, we consider the challenging scenario where the AP-IRS channel is rank-one or approximately rank-one, i.e., $\mathrm{rank}(\boldsymbol{G}) = 1$. Nevertheless, as discussed later in this paper, our proposed algorithm can be readily adapted to the less challenging scenario where the rank of the AP-IRS channel is greater than one.

B. Signal Model

1) Transmit Signal Model: In this paper, we employ OFDM signals to probe potential targets. The advantage of using

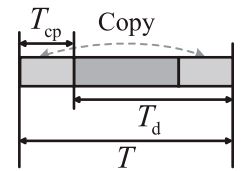


Fig. 2. One complete OFDM block.

OFDM signals for sensing lies in its ability in mitigating possible fading and providing additional frequency diversity, as different scattering centers of a target resonate at different frequencies [27], [28], [29], [30], [31]. Moreover, since OFDM is widely adopted in communication systems, using OFDM signals for sensing can help realize sensing and communication functionality on a same hardware platform [32], [33], [34], [35]. Specifically, in a coherent processing interval (CPI), the AP transmits a train of *P* uniformly-spaced OFDM pulses. In each pulse, the AP transmits one OFDM block and then receives the echo form potential targets. Here we assume the AP operates in a half-duplex mode, i.e., at any given time instant, it can only either transmit signals or receive echo signals. Thus, the AP, when receiving its echo signal, will not be interfered by its own transmitted signals.

Suppose there are L orthogonal subcarriers in each block and the subcarrier spacing is set as $\Delta f = 1/T_{\rm d}$. The duration of one block is $T = T_{\rm cp} + T_{\rm d}$, where $T_{\rm cp}$ is the length of the cyclic prefix and $T_{\rm d}$ is the duration of an OFDM symbol. The cyclic prefix is a replica of the end part of the OFDM symbol (see Fig. 2). Note in communications, the duration of the cyclic prefix, $T_{\rm cp}$, should be larger than the time dispersion in a radio channel with multipath propagation in order to avoid the inter-symbol interference (ISI). While in this paper, the length of cyclic prefix determines the maximum sensing distance from the IRS to the target, which will be elaborated later.

Define $T_{\rm PRI}$ as the pulse repetition interval (PRI). The baseband signal in the pth pulse can be expressed as

$$s_p(t) = \sum_{l=1}^{L} \beta_l e^{j2\pi l\Delta f t} \xi(t - pT_{\text{PRI}}) \tag{4}$$

where $pT_{\text{PRI}} \leq t \leq pT_{\text{PRI}} + T$, $\xi(t)$ is the rectangular function that takes 1 for $t \in [0,T]$ and 0 otherwise [29], and β_l is the unit-energy modulated symbol which satisfies $|\beta_l|^2 = 1$, $\forall l$. For such a signal, it can be readily verified that the cyclic prefix part is a repetition of the end part of the OFDM block for any $T_{\text{cp}} = \mu T$, $1 > \mu > 0$. Also, for simplicity, we assume $\beta_l = \beta$, $\forall l$ in this paper. Suppose we use an individual transmit beamforming vector $\boldsymbol{w}_p \in \mathbb{C}^M$ to transmit the pth pulse. Then the transmitted signal can be expressed as

$$\boldsymbol{x}_p(t) = \sqrt{P_t} \boldsymbol{w}_p s_p(t) \exp(j2\pi f_c t)$$
 (5)

where P_t denotes the transmit power and f_c denotes the carrier frequency.

2) Received Signal Model: Assume that the kth target is located at a distance of R_k meters (m) from the IRS and the target

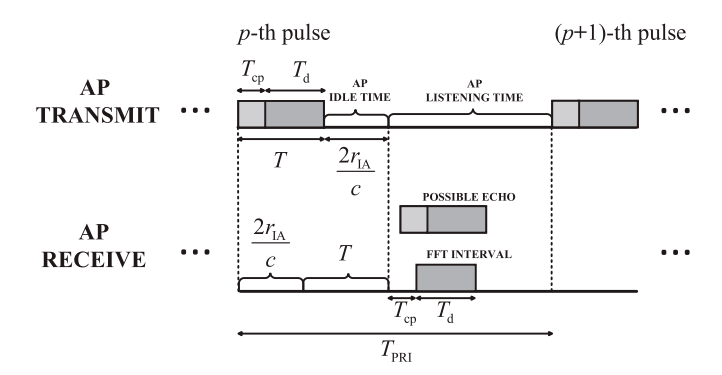


Fig. 3. A schematic of signal transmission in one pulse repetition interval.

is moving towards the IRS with a radial velocity of v_k (m/s). In each PRI, the reception during the interval $[0,T+2r_{\rm IA}/c]$ is inhibited to avoid the interference signal directly reflected from the IRS (see Fig. 3), and the AP starts to listen to its echo signal at time $T+2r_{\rm IA}/c$. Here T is the duration of the transmitted pulse, and $2r_{\rm IA}/c$ is the time for a radar signal to travel to the IRS and back to the AP. This guard interval also determines the minimum sensing distance from the target to the IRS, which will be elaborated in the next section. Also, we make the following assumption in order to acquire the complete echo signal reflected from the targets.

Assumption 1: The echo signals from all potential targets are assumed to lie within the interval of $[2r_{\rm IA}/c + T, 2r_{\rm IA}/c + 2T + T_{\rm cp}]$.

Below we explain why we assume the echo signals lie within the i nterval $[2r_{\rm IA}/c+T,2r_{\rm IA}/c+2T+T_{\rm cp}]$. Note that our proposed algorithm starts by taking a Fourier transform of the received signal over a time window of length $T_d=T-T_{\rm cp}$ (cf. (8)). This time window cannot be arbitrarily placed. Instead, it has to be placed at an appropriate place to process both the earliest possible echo signal and the latest possible echo signal. Recall that, to avoid collision, the earliest possible echo signal is assumed to arrive at the AP over the interval $[2r_{\rm IA}/c+T,2r_{\rm IA}/c+2T]$. To process this earliest echo signal without any information lost, the latest time point from which this time window starts is $2r_{\rm IA}/c+T+T_{\rm cp}$. In other words, this time window should be placed over the interval $[2r_{\rm IA}/c+T+T_{\rm cp},2r_{\rm IA}/c+2T]$. Note that since the cyclic prefix part is

a replica of the end part of the OFDM block, the information of the earliest echo signal remains complete over the interval $[2r_{\rm IA}/c+T+T_{\rm cp},2r_{\rm IA}/c+2T]$. From this time window, we know that the latest possible echo signal that can be processed by the AP starts at time $2r_{\rm IA}/c+T+T_{\rm cp}$ and ends at $2r_{\rm IA}/c+2T+T_{\rm cp}$. If the echo signal arrives at the AP after this time point $2r_{\rm IA}/c+T+T_{\rm cp}$, the information of this echo signal will be lost. From the above analysis, we know that the echo signals have to lie within the interval $[2r_{\rm IA}/c+T,2r_{\rm IA}/c+2T+T_{\rm cp}]$.

Based on Assumption 1, the pulse repetition interval needs to satisfy $T_{\rm PRI} \geq 2r_{\rm IA}/c + 2T + T_{\rm cp}$. Since the AP operates in a listening mode within the interval $[2r_{\rm IA}/c + T, T_{\rm PRI}]$, the received echo signal only contains signals reflected by targets. Thus, for the pth pulse, the received signal at the mth antenna of the AP can be written as

$$\tilde{y}_{p,m}(t) = \sum_{k=1}^{K} \boldsymbol{g}_{m}^{T} \boldsymbol{\Phi}^{T} \boldsymbol{H}_{k} \boldsymbol{\Phi} \boldsymbol{G} \boldsymbol{x}_{p}(t - \tau_{p,k}) + \tilde{n}_{p,m}(t)$$
(6)

where ${m g}_m$ is the mth column of ${m G}$, ${m au}_{p,k}=rac{2(R_k+r_{\rm IA}-v_kpT_{\rm PRI})}{c}$ is the round-trip time delay associated with the kth target, c is the speed of light and $\tilde{n}_{p,m}(t)$ is the additive Gaussian noise. For notational simplicity, we define ${m au}_k\triangleq \frac{2R_k}{c}$, ${\nu}_k\triangleq \frac{2v_kf_c}{c}$ and ${\tau}_0\triangleq \frac{2r_{\rm IA}}{c}$. We have ${\tau}_{p,k}={\tau}_k+{\tau}_0-{\nu}_kpT_{\rm PRI}/f_c$.

After removing the carrier frequency, the baseband signal can be written as (7) shown at the bottom of the page, where $\bar{\alpha}_k \triangleq \sqrt{P_t} \tilde{\alpha}_k e^{-j2\pi f_c(\tau_k + \tau_0)}, \ \ b_m(\theta_k) \triangleq \boldsymbol{g}_m^T \boldsymbol{\Phi}^T \boldsymbol{a}(\theta_k), \ \ z_p(\theta_k, \nu_k) \triangleq \boldsymbol{a}^T(\theta_k) \boldsymbol{\Phi} \boldsymbol{G} \boldsymbol{w}_p e^{j2\pi p T_{\text{PRI}}\nu_k}$ and $\bar{n}_{p,m}(t)$ is the baseband noise.

Taking the Fourier transform of the received pth pulse baseband signal over the interval $[2r_{\rm IA}/c + T + T_{\rm cp}, 2r_{\rm IA}/c + 2T]$ (note that $\tau_0 = 2r_{\rm IA}/c$), the signal associated with the lth subcarrier is given by

$$\tilde{y}_{p,m}[l] = \int_{pT_{\text{PRI}} + \tau_0 + T + T_{\text{cp}}}^{pT_{\text{PRI}} + \tau_0 + 2T} \bar{y}_{p,m}(t) e^{-j2\pi l \Delta f t} dt \qquad (8)$$

Plugging (4) and (7) into (8), we have (9) shown at the bottom of the next page, where the approximation (a) follows from the fact that the bandwidth of the baseband signal is far less than the carrier frequency, i.e., $L\Delta f \ll f_c$, and (b) is due to the subcarrier orthogonality [32], i.e.

$$\int_{pT_{\rm PRI}+\tau_0+T+T_{\rm cp}}^{pT_{\rm PRI}+\tau_0+2T} e^{j2\pi(l\Delta f-q\Delta f)t} dt = T_{\rm d}\delta(q\Delta f-l\Delta f) \ \ (10)$$

$$\bar{y}_{p,m}(t) = \sum_{k=1}^{K} \sqrt{P_{t}} \tilde{\alpha}_{k} \boldsymbol{g}_{m}^{T} \boldsymbol{\Phi}^{T} \boldsymbol{a}(\theta_{k}) \boldsymbol{a}^{T}(\theta_{k}) \boldsymbol{\Phi} \boldsymbol{G} \boldsymbol{w}_{p} s_{p}(t - \tau_{p,k}) e^{-j2\pi f_{c}\tau_{p,k}} + \bar{n}_{p,m}(t)$$

$$= \sum_{k=1}^{K} \sqrt{P_{t}} \tilde{\alpha}_{k} \boldsymbol{g}_{m}^{T} \boldsymbol{\Phi}^{T} \boldsymbol{a}(\theta_{k}) \boldsymbol{a}^{T}(\theta_{k}) \boldsymbol{\Phi} \boldsymbol{G} \boldsymbol{w}_{p} s_{p}(t - \tau_{p,k}) e^{j2\pi p T_{\text{PRI}}\nu_{k}} e^{-j2\pi f_{c}(\tau_{k} + \tau_{0})} + \bar{n}_{p,m}(t)$$

$$= \sum_{k=1}^{K} \bar{\alpha}_{k} \boldsymbol{g}_{m}^{T} \boldsymbol{\Phi}^{T} \boldsymbol{a}(\theta_{k}) \boldsymbol{a}^{T}(\theta_{k}) \boldsymbol{\Phi} \boldsymbol{G} \boldsymbol{w}_{p} s_{p}(t - \tau_{p,k}) e^{j2\pi p T_{\text{PRI}}\nu_{k}} + \bar{n}_{p,m}(t)$$

$$= \sum_{k=1}^{K} \bar{\alpha}_{k} b_{m}(\theta_{k}) z_{p}(\theta_{k}, \nu_{k}) s_{p}(t - \tau_{p,k}) + \bar{n}_{p,m}(t)$$
(7)

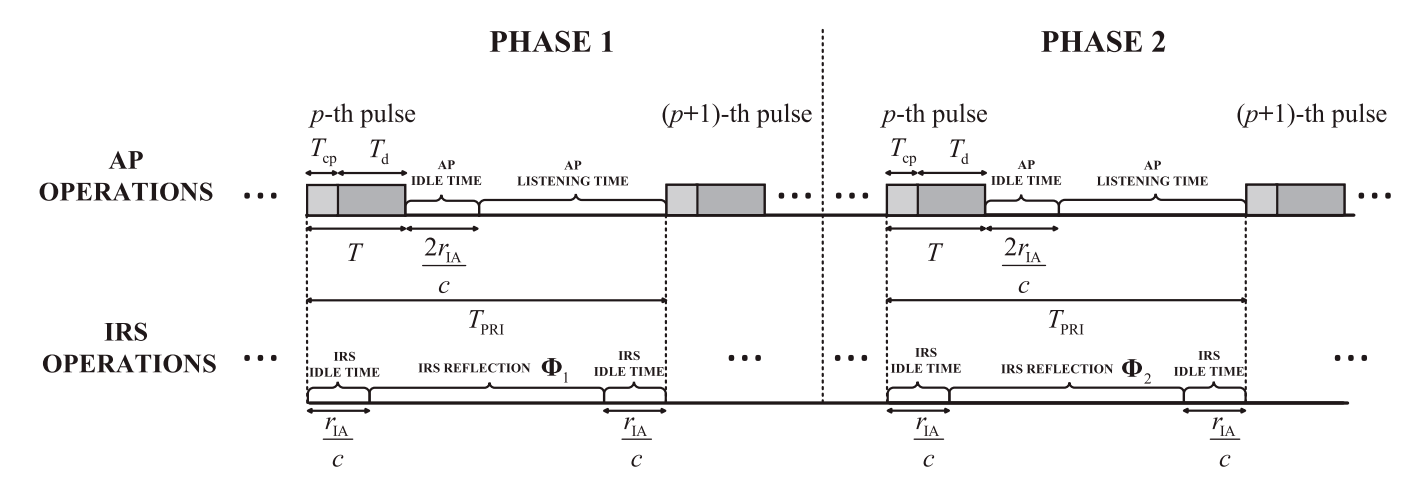


Fig. 4. A schematic of signal transmission for the two-phase NLOS sensing scheme.

Define $\alpha_k \triangleq \bar{\alpha}_k \beta T_d$, and ignore the common phase term τ_0 in (9) as this term is known *a priori*, we have

$$y_{p,m}[l] = \sum_{k=1}^{K} \alpha_k b_m(\theta_k) z_p(\theta_k, \nu_k) e^{-j2\pi l \Delta f \tau_k} + n_{p,m}[l]$$
(11)

where

$$n_{p,m}[l] = \int_{pT_{\rm PRI} + \tau_0 + T + T_{\rm cp}}^{pT_{\rm PRI} + \tau_0 + 2T} \bar{n}_{p,m}(t) e^{-j2\pi l \Delta f t} dt \qquad (12)$$

It is assumed that $n_{p,m}[l]$ is a complex Gaussian variable with zeros mean and variance σ^2 , i.e., $n_{p,m}[l] \sim \mathcal{CN}(0, \sigma^2)$.

III. PROPOSED SENSING SCHEME AND CP DECOMPOSITION

A. Two-Phase Sensing Scheme

The proposed two-phase sensing scheme is illustrated in Fig. 4, in which the entire sensing cycle is divided into two phases, say, phase 1 and phase 2, and each of them is assigned an individual IRS phase-shift profile. In each phase, the AP transmits P pulses in total. The pulse repetition interval is $T_{\rm PRI}$, and the interval between the Pth pulse in phase 1 and the first pulse in phase 2 is also set to $T_{\rm PRI}$.

In the following, we first analyze the minimum sensing distance $R_{\rm min}$, the maximum sensing distance $R_{\rm max}$ and the maximum unambiguous velocity $v_{\rm max}$ with respect to the IRS.

1) Minimum Sensing Distance: To avoid the collision with the self-interference and the signal reflected directly from the IRS, the reception is inhibited for the AP during the interval $[pT_{\rm PRI}, pT_{\rm PRI} + 2r_{\rm IA}/c + T]$. In other words, we assume that the earliest possible echo signal arrives at the AP at time $t_0 \triangleq T + 2r_{\rm IA}/c$. This assumption implies that there is a requirement on the minimum distance between the target and the IRS, which is referred to as the minimum sensing distance in our paper and can be easily calculated as

$$R_{\min} = \frac{cT}{2} \tag{13}$$

2) Maximum Sensing Distance: According to Assumption 1, we know that the latest possible echo signal reflected by a potential target will be received within the interval $[2r_{\rm IA}/c + T + T_{\rm cp}, 2r_{\rm IA}/c + 2T + T_{\rm cp}]$. As a result, the maximum sensing distance with respect to the IRS is given by

$$R_{\text{max}} \le \frac{c(T + T_{\text{cp}})}{2} \tag{14}$$

Notably, to cover the latest possible echo signal, the PRI has to be greater than $T_{\rm PRI} \geq 2r_{\rm IA}/c + 2T + T_{\rm cp}$. If we choose $T_{\rm PRI} =$

$$\tilde{y}_{p,m}[l] = \int_{pT_{\text{PRI}}+\tau_0+T+T_{\text{cp}}}^{pT_{\text{PRI}}+\tau_0+2T} e^{-j2\pi l\Delta ft} \sum_{k=1}^{K} \bar{\alpha}_k b_m(\theta_k) z_p(\theta_k, \nu_k) \sum_{q=1}^{L} \beta e^{j2\pi q\Delta f(t-\tau_{p,k})} dt + n_{p,m}[l] \\
= \sum_{k=1}^{K} \bar{\alpha}_k b_m(\theta_k) z_p(\theta_k, \nu_k) \int_{pT_{\text{PRI}}+\tau_0+T+T_{\text{cp}}}^{pT_{\text{PRI}}+\tau_0+2T} e^{-j2\pi l\Delta ft} \sum_{q=1}^{L} \beta e^{j2\pi q\Delta f(t-\tau_k-\tau_0)} e^{j2\pi \frac{q\Delta f}{fc} pT_{\text{PRI}}\nu_k} dt + n_{p,m}[l] \\
\stackrel{(a)}{\approx} \sum_{k=1}^{K} \bar{\alpha}_k b_m(\theta_k) z_p(\theta_k, \nu_k) \int_{pT_{\text{PRI}}+\tau_0+T+T_{\text{cp}}}^{pT_{\text{PRI}}+\tau_0+2T} e^{-j2\pi l\Delta ft} \sum_{q=1}^{L} \beta e^{j2\pi q\Delta f(t-\tau_k-\tau_0)} dt + n_{p,m}[l] \\
\stackrel{(b)}{=} \beta T_{\text{d}} \sum_{k=1}^{K} \bar{\alpha}_k b_m(\theta_k) z_p(\theta_k, \nu_k) e^{-j2\pi l\Delta f(\tau_k+\tau_0)} + n_{p,m}[l] \tag{9}$$

 $2r_{\rm IA}/c + 2T + T_{\rm cp}$, we see that the maximum sensing distance is determined by $T_{\rm PRI} - T$.

3) Unambiguous Velocity: The maximum unambiguous velocity characterizes the maximum detectable radial velocity of a target with respect to the IRS. The radial velocity can be uniquely determined if there is no phase ambiguity in $e^{j2\pi T_{\text{PRI}}\nu_k}$, i.e., $T_{\text{PRI}}\nu_k \leq 1$. Recalling $\nu_k \triangleq \frac{2v_k f_c}{c}$, the maximum unambiguous velocity can be given as

$$v_{\text{max}} \le \frac{c}{2f_c T_{\text{PRI}}} \tag{15}$$

B. Tensor Representation

Based on the above two-phase sensing scheme, we now show how to formulate the received signals into tensors. Specifically, let Φ_1 and Φ_2 , respectively, denote the IRS phase shift matrices employed in phase 1 and phase 2. Define

$$b_{i,m}(\theta_k) \triangleq \boldsymbol{g}_m^T \boldsymbol{\Phi}_i^T \boldsymbol{a}(\theta_k) \tag{16}$$

$$z_{i,p}(\theta_k, \nu_k) \triangleq \boldsymbol{a}^T(\theta_k) \boldsymbol{\Phi}_i \boldsymbol{G} \boldsymbol{w}_p e^{j2\pi p T_{\text{PRI}} \nu_k}$$
 (17)

where $i \in \{1,2\}$. We first consider the signals received in phase 1. For each subcarrier l, stacking the received echo signal from all P pulses and all M antennas, we can construct a matrix $\mathbf{Y}_1(l) \in \mathbb{C}^{P \times M}$, with its (p,m)th entry denoted by $[\mathbf{Y}_1(l)]_{p,m} = y_{p,m}^1[l]$ and given as (11)

$$y_{p,m}^{1}[l] = \sum_{k=1}^{K} \alpha_k b_{1,m}(\theta_k) \times z_{1,p}(\theta_k, \nu_k) e^{-j2\pi l \Delta f \tau_k} + n_{1,p,m}[l]$$
(18)

Consequently, we have

$$\boldsymbol{Y}_{1}(l) = \sum_{k=1}^{K} \alpha_{k} f_{l}(\tau_{k}) \boldsymbol{z}_{1}(\theta_{k}, \nu_{k}) \boldsymbol{b}_{1}^{H}(\theta_{k}) + \boldsymbol{N}_{1,l}$$
(19)

where
$$\mathbf{z}_1(\theta_k, \nu_k) \triangleq [z_{1,1}(\theta_k, \nu_k) \cdots z_{1,P}(\theta_k, \nu_k)]^T \in \mathbb{C}^P$$
, $\mathbf{b}_1(\theta_k) \triangleq [b_{1,1}(\theta_k) \cdots b_{1,M}(\theta_k)] \in \mathbb{C}^M$, and $f_l(\tau_k) \triangleq e^{-j2\pi l\Delta f \tau_k}$.

Now consider the signals received in phase 2. In phase 1, the distance between the kth target and the IRS is denoted as R_k . When it comes to phase 2, the distance between the target and the IRS has changed to $\tilde{R}_k=R_k+\Delta r_k$, where $\Delta r_k=v_kPT_{\rm PRI}$ is the shift of distance during the time interval between two phases. For a typical sensing scenario, suppose the velocity of the target is $v=120\,{\rm km/h}$, the number of pulses is set to P=100 and the PRI is set to $T_{\rm PRI}=10\,\mu{\rm s}$. We have $\Delta r_k=vPT_{\rm PRI}\approx 0.03\,{\rm m}$. This distance shift generally has a very slight influence on the distance-dependent path loss and the target's DOA with respect to IRS. Therefore, in phase 2, it is reasonable to assume that the path loss α , the target's DOA θ , as well as the time delay τ remain the same as in phase 1. The received signals in phase 2 can be written as

$$y_{p,m}^{2}[l] = \sum_{k=1}^{K} \alpha_{k} b_{2,m}(\theta_{k})$$

$$\times z_{2,p}(\theta_{k}, \nu_{k}) e^{-j2\pi l \Delta f \tau_{k}} + n_{2,p,m}[l]$$
(20)

During phase 2, let $\boldsymbol{Y}_2(l) \in \mathbb{C}^{P \times M}$ denote the matrix constructed by stacking the received echo signal from all P pulses and all M antennas for each subcarrier l. We have

$$\boldsymbol{Y}_{2}(l) = \sum_{k=1}^{K} \alpha_{k} f_{l}(\tau_{k}) \boldsymbol{z}_{2}(\theta_{k}, \nu_{k}) \boldsymbol{b}_{2}^{H}(\theta_{k}) + \boldsymbol{N}_{2,l}$$
(21)

where $\mathbf{z}_2(\theta_k, \nu_k) \triangleq [z_{2,1}(\theta_k, \nu_k) \cdots z_{2,P}(\theta_k, \nu_k)]^T \in \mathbb{C}^P$, $\mathbf{b}_2(\theta_k) \triangleq [b_{2,1}(\theta_k) \cdots b_{2,M}(\theta_k)] \in \mathbb{C}^M$, $f_l(\tau_k) = e^{-j2\pi l\Delta f \tau_k}$ and $\mathbf{N}_{2,l}$ is the additive Gaussian noise.

For phase i, by concatenating the received signals across L subcarriers, we can naturally obtain a third-order tensor $\mathbf{\mathcal{Y}}_i \in \mathbb{C}^{P \times M \times L}$, with its (p,m,l)th entry given by $[\mathbf{Y}_i(l)]_{p,m}$, whose three modes respectively stand for the pulses, the AP's antennas and the subcarriers. Note that each slice of the tensor $\mathbf{\mathcal{Y}}_i$ is $\mathbf{Y}_i(l)$, which is a weighted sum of a common set of rank-one outer products. Therefore the tensor $\mathbf{\mathcal{Y}}_i$ admits a CP decomposition as

$$\boldsymbol{\mathcal{Y}}_{i} = \sum_{k=1}^{K} \boldsymbol{z}_{i}(\theta_{k}, \nu_{k}) \circ \boldsymbol{b}_{i}(\theta_{k}) \circ \alpha_{k} \boldsymbol{f}(\tau_{k}) + \boldsymbol{\mathcal{N}}_{i}$$
(22)

where o denotes the outer product, and we have

$$\mathbf{f}(\tau_k) \triangleq [e^{-j2\pi\Delta f \tau_k} \cdots e^{-j2\pi L\Delta f \tau_k}]^T \tag{23}$$

$$\boldsymbol{b}_i(\theta) = \boldsymbol{G}^T \boldsymbol{\Phi}_i \boldsymbol{a}(\theta) \tag{24}$$

$$\boldsymbol{z}_{i}(\theta, \nu) = (\boldsymbol{W}^{T} \boldsymbol{G}^{T} \boldsymbol{\Phi}_{i} \boldsymbol{a}(\theta)) \otimes (\boldsymbol{d}(\nu))$$
 (25)

in which $\boldsymbol{W} \triangleq [\boldsymbol{w}_1 \ \cdots \ \boldsymbol{w}_P] \in \mathbb{C}^{M \times P}, \quad \boldsymbol{d}(\nu) \triangleq [e^{j2\pi T_{\mathrm{PRI}}\nu} \ \cdots \ e^{j2\pi P T_{\mathrm{PRI}}\nu}]^T \in \mathbb{C}^P \quad \text{and} \quad \circledast \quad \text{denotes} \quad \text{the Hadamard product.}$

Define

$$\mathbf{A}_i \triangleq [\mathbf{z}_i(\theta_1, \nu_1) \quad \cdots \quad \mathbf{z}_i(\theta_K, \nu_K)] \in \mathbb{C}^{P \times K}$$
 (26)

$$\boldsymbol{B}_i \triangleq [\boldsymbol{b}_i(\theta_1) \cdots \boldsymbol{b}_i(\theta_K)] \in \mathbb{C}^{M \times K}$$
 (27)

$$C \triangleq [\alpha_1 \mathbf{f}(\tau_1) \cdots \alpha_K \mathbf{f}(\tau_K)] \in \mathbb{C}^{L \times K}$$
 (28)

Here $\{A_i, B_i, C\}$ are the factor matrices of the tensor \mathcal{Y}_i , where $i \in \{1, 2\}$. We see that the factor matrices contain information about the DOAs, Doppler shifts and time delays of the targets. Leveraging the two phases' observations, we, in the following, develop a two-stage method which first estimates the factor matrices of the tensor \mathcal{Y}_i and then jointly recovers the target's DOAs, time delays and Doppler shifts based on the estimated factor matrices. Before proceeding, we first discuss the uniqueness of CP decomposition as it plays a crucial role in the identifiability of the proposed method.

C. Identifiability Condition

A well-known condition to ensure the uniqueness of CP decomposition is Kruskal's condition [36], [37], [38], i.e.

$$k_{\mathbf{A}^{(1)}} + k_{\mathbf{A}^{(2)}} + k_{\mathbf{A}^{(3)}} \ge 2R + 2$$
 (29)

where $A^{(1)} \in \mathbb{C}^{I \times R}$, $A^{(2)} \in \mathbb{C}^{J \times R}$ and $A^{(3)} \in \mathbb{C}^{K \times R}$ are factor matrices associated with the third-order tensor $\mathcal{X} \in \mathbb{C}^{I \times J \times K}$. k_A denotes the k-rank of a matrix A, which is defined as the largest value of k_A such that every subset of k_A columns of the matrix A is linearly independent.

For our problem, recall that $b_i(\theta) = G^T \Phi_i a(\theta)$, and G is a rank-one matrix. Writing $G = \sigma u v^T$, we have $b_i(\theta) = c_i(\theta) v$, where $c_i(\theta) = \sigma u^T \Phi_i a(\theta)$ is a scalar. Therefore, we can see that columns of the factor matrix B_i are linearly dependent. Thus, we have $k_{B_i} = 1$. In this case, even A_i and C are full k-rank, the Kruskal's condition cannot be satisfied.

Meanwhile, we notice that the factor matrix C has a Vandermonde structure. Previous studies found that, when one of the factor matrices, say $A^{(3)}$ has a Vandermonde structure, the uniqueness of the CP decomposition can be guaranteed if the following conditions are satisfied [39], [40]:

$$\begin{cases} \operatorname{rank} \left(\underline{\mathbf{A}}^{(3)} \odot \mathbf{A}^{(2)} \right) = R \\ \operatorname{rank} \left(\mathbf{A}^{(1)} \right) = R \end{cases}$$
 (30)

where \underline{A} represents a sub-matrix of A that is obtained by removing the bottom row of A, and \odot denotes the Khatri-Rao product.

From the above condition (30), we know that for each i, if

$$\begin{cases} \operatorname{rank} \left(\underline{C} \odot B_i \right) = K \\ \operatorname{rank} \left(A_i \right) = K \end{cases}$$
(31)

then the CP decomposition of \mathcal{Y}_i is essentially unique.

Note that different targets usually have different distances from the IRS, C is thus a Vandermonde matrix with distinct generators $\{e^{-j2\pi\Delta f\tau_k}\}$. According to [39], we can arrive at $\mathrm{rank}(\underline{C}\odot B_i)=K$ even if matrix B_i has redundant columns, provided that $(L-1)M\geq K$.

Recall $b_i(\theta) = G^T \Phi_i a(\theta) = c_i(\theta) v$. Therefore the column of the factor matrix A_i can be expressed as

$$\mathbf{z}_{i}(\theta, \nu) = (\mathbf{W}^{T} \mathbf{G}^{T} \mathbf{\Phi}_{i} \mathbf{a}(\theta)) \circledast (\mathbf{d}(\nu))$$

$$= (\mathbf{W}^{T} \mathbf{b}_{i}(\theta)) \circledast (\mathbf{d}(\nu))$$

$$= (c_{i}(\theta) \mathbf{W}^{T} \mathbf{v}) \circledast (\mathbf{d}(\nu))$$
(32)

In practice, different targets are usually associated with different Doppler shifts. From (32), we know that A_i is obtained from a Vandermonde matrix multiplied columnwisely by a same vector with different scaling factors. Hence for a generic $W^T v$, A_i is full rank and we have $\operatorname{rank}(A_i) = \min\{P, K\}, \forall i$.

In summary, we have the following proposition concerning the uniqueness of the CP decomposition.

Proposition 1: Assume that the delay and Doppler shift parameters associated with different targets are different. The uniqueness condition of CP decomposition can be guaranteed almost surely when both $(L-1)M \geq K$ and $P \geq K$ are satisfied.

D. CP Decomposition

We now discuss how to perform CP decomposition by utilizing the Vandermonde structure of the factor matrix. Such a method was originally proposed in [39]. To make the paper self-contained, we provide a brief description of the CP decomposition method.

To ease our presentation, we drop the subscript i in the tensor and the associated factor matrices. The mode-1 unfolding of ${\cal Y}$ can be written as

$$\mathbf{\mathcal{Y}}_{(1)}^{T} = (\mathbf{C} \odot \mathbf{B}) \mathbf{A}^{T} + \mathbf{\mathcal{N}}_{(1)}^{T}$$
(33)

Ignoring the noise, we can compute the truncated singular value decomposition (SVD) of the noiseless $\mathbf{\mathcal{Y}}_{(1)}^T \in \mathbb{C}^{LM \times P}$ as

$$\mathbf{\mathcal{Y}}_{(1)}^{T} = U \mathbf{\Sigma} V^{H} \tag{34}$$

where $U \in \mathbb{C}^{LM \times K}$, $\Sigma \in \mathbb{C}^{K \times K}$ and $V \in \mathbb{C}^{P \times K}$. If the uniqueness condition (31) is satisfied, there exists a nonsingular matrix $R \in \mathbb{C}^{K \times K}$ such that

$$UR = C \odot B \tag{35}$$

Define $U_1=[U]_{1:(L-1)M,:}\in\mathbb{C}^{(L-1)M imes K}$ and $U_2=[U]_{M+1:LM,:}\in\mathbb{C}^{(L-1)M imes K}.$ We have

$$U_1 R = C \odot B \tag{36}$$

$$U_2 R = \overline{C} \odot B \tag{37}$$

where \overline{C} represents a submatrix of C by removing the top row of C, and \underline{C} represents a submatrix of C by removing the bottom row of C. Utilizing the Vandermonde structure of C, we have

$$(C \odot B) T = \overline{C} \odot B \tag{38}$$

in which $T = \text{diag}(t_1, \dots, t_K)$ and $t_k \triangleq e^{-j2\pi \Delta f \tau_k}$. Combining (36)–(38), we obtain

$$U_2R = U_1RT \tag{39}$$

According to (31) and (35), both U_1 and U_2 are full column rank. Hence we can rewrite (39) as

$$\boldsymbol{U}_{1}^{\dagger}\boldsymbol{U}_{2} = \boldsymbol{R}\boldsymbol{T}\boldsymbol{R}^{-1} \tag{40}$$

Thus, we can perform the eigenvalue decomposition (EVD) of $U_1^{\dagger}U_2$ to estimate T and the associated generators $\{t_k\}_{k=1}^K$. We can reconstruct the columns $\{\hat{c}_k\}$ of \hat{C} by

$$\hat{\boldsymbol{c}}_k = [\hat{t}_k \quad \hat{t}_k^2 \quad \cdots \quad \hat{t}_k^L] \tag{41}$$

Based on (35) and the reconstructed \hat{C} , the column of the factor matrix \hat{B} can be estimated as

$$\hat{\boldsymbol{b}}_{k} = \left(\frac{\hat{\boldsymbol{c}}_{k}^{H}}{\hat{\boldsymbol{c}}_{k}^{H}\hat{\boldsymbol{c}}_{k}} \otimes \boldsymbol{I}_{M}\right) \boldsymbol{U}[\boldsymbol{R}]_{:,k} \tag{42}$$

Finally, given \hat{B} and \hat{C} , the factor matrix A can be estimated as

$$\hat{A} = \mathcal{Y}_{(1)} \left(\left(\hat{C} \odot \hat{B} \right)^T \right)^{\dagger} \tag{43}$$

After we obtain the estimated factor matrices \hat{A} , \hat{B} and \hat{C} , we, in Section IV, discuss how to extract the sensing parameters from the estimated factor matrices.

E. Generating IRS Coefficients Φ_1 and Φ_2

Note that our proposed method relies on leveraging the diversity in the illumination pattern of the IRS across different phases. In fact, the IRS phase-shift profiles Φ_1 and Φ_2 can be arbitrarily chosen as long as they are sufficiently distinct from each other. Here we introduce a simple scheme to generate Φ_1 and Φ_2 . Specifically, we partition the IRS into a number

of subarrays, say, 4 subarrays. For each subarray, its reflection coefficients are set to form a directional beam pointing to a certain direction. Particularly, if the target's DOA is within a range that is known a priori, i.e. $\theta_k \in [\theta^{\mathrm{lb}}, \theta^{\mathrm{ub}}]$, we can let different subarrays create multiple directional beams that collectively cover this wide range of directions $[\theta^{\mathrm{lb}}, \theta^{\mathrm{ub}}]$. Also, each subarray, in two different phases, steers its beam towards different directions. In doing this way, the illumination patterns of the IRS in two phases are thus different.

IV. TARGET PARAMETER ESTIMATION

After CP decomposition, we now have access to the estimated factor matrices $\{\hat{A}_i, \hat{B}_i, \hat{C}_i\}$, in which $i \in \{1, 2\}$. Note that for both phases, the factor matrix C_i remains the same, i.e. $C_1 = C_2 = C$. Due to the inherent permutation and scaling ambiguities, the estimated factor matrices are related with the true factor matrices as

$$\begin{cases}
\hat{A}_1 = A_1 \Lambda_1 \Pi_1 + E_1 \\
\hat{B}_1 = B_1 \Lambda_2 \Pi_1 + E_2 \\
\hat{C}_1 = C \Lambda_3 \Pi_1 + E_3
\end{cases}$$
(44)

and

$$\begin{cases}
\hat{A}_{2} = A_{2}\Gamma_{1}\Pi_{2} + \tilde{E}_{1} \\
\hat{B}_{2} = B_{2}\Gamma_{2}\Pi_{2} + \tilde{E}_{2} \\
\hat{C}_{2} = C\Gamma_{2}\Pi_{2} + \tilde{E}_{2}
\end{cases}$$
(45)

where $\{\Lambda_1, \Lambda_2, \Lambda_3, \}$ and $\{\Gamma_1, \Gamma_2, \Gamma_3, \}$ are unknown nonsingular diagonal matrices satisfying $\Lambda_1\Lambda_2\Lambda_3 = I$ and $\Gamma_1\Gamma_2\Gamma_3 = I$, $\{\Pi_i\}$ are unknown permutation matrices, $\{E_1, E_2, E_3\}$ and $\{\tilde{E}_1, \tilde{E}_2, \tilde{E}_3\}$ are estimation errors.

A. The Scaling Ambiguity Issue

First, we show that, when only a single phase is considered, why the DOA estimation is infeasible in the scenario of $\operatorname{rank}(G)=1$. Recall that $\boldsymbol{b}_i(\theta)=\boldsymbol{G}^T\boldsymbol{\Phi}_i\boldsymbol{a}(\theta)$. Hence, we can write $\boldsymbol{B}_i=\boldsymbol{G}^T\boldsymbol{\Phi}_i\boldsymbol{\Xi}$, where $\boldsymbol{\Xi}\triangleq[\boldsymbol{a}(\theta_1)\cdots\boldsymbol{a}(\theta_K)]\in\mathbb{C}^{N\times K}$. If the rank of the channel matrix \boldsymbol{G} is greater than one, then we can employ a correlation-based method [41] to extract the parameter θ_k from each column of $\hat{\boldsymbol{B}}_1$, i.e.,

$$\hat{\theta}_{k} = \underset{\theta_{k}}{\arg \max} \frac{|\hat{\boldsymbol{b}}_{1,k}^{H} \boldsymbol{b}_{1}(\theta_{k})|}{\|\hat{\boldsymbol{b}}_{1,k}\|_{2} \|\boldsymbol{b}_{1}(\theta_{k})\|_{2}}$$
(46)

where $\hat{\boldsymbol{b}}_{1,k}$ is the kth column of $\hat{\boldsymbol{B}}_1$. In this case, only using the received signals from a single phase suffices to recover parameters of interest. Nevertheless, this method fails when $\mathrm{rank}(\boldsymbol{G})=1$. The reason can be explained as follows. Specifically, when $\mathrm{rank}(\boldsymbol{G})=1$, \boldsymbol{G} can be expressed as $\boldsymbol{G}=\sigma\boldsymbol{u}\boldsymbol{v}^T$. In this case, we have $\hat{\boldsymbol{B}}_1=\sigma\boldsymbol{v}\boldsymbol{u}^T\boldsymbol{\Phi}_1\boldsymbol{\Xi}\boldsymbol{\Lambda}_2$, where, for simplicity, the unknown permutation matrix and the estimation error are neglected. The kth column of $\hat{\boldsymbol{B}}_1$ is thus given by

$$\hat{\boldsymbol{b}}_{1.k} = \sigma \boldsymbol{v} \boldsymbol{u}^T \boldsymbol{\Phi}_1 \boldsymbol{a}(\theta_k) [\boldsymbol{\Lambda}_2]_{k.k} \tag{47}$$

where $[\Lambda_2]_{k,k}$ denotes the kth diagonal element of Λ_2 . Here $u^T \Phi_1 a(\theta_k) [\Lambda_2]_{k,k}$ is a complex scalar. Due to the coupling

between the unknown scalar $u^T \Phi_1 a(\theta_k)$ and the unknown scalar $[\Lambda_2]_{k,k}$, the parameter θ_k cannot be uniquely identified.

From the above discussion, we see that when $\mathrm{rank}(G)=1$, using the factor matrices $\{\hat{A}_1,\hat{B}_1,\hat{C}_1\}$ obtained from the first phase alone cannot uniquely identify the targets' parameters. In the following, we will show how to utilize the estimated factor matrices from two different phases to resolve this ambiguity.

B. Column Alignment for Factor Matrices

To leverage the estimated factor matrices, we first remove the permutation ambiguity between phase 1 and phase 2. Notice that both \hat{C}_1 and \hat{C}_2 are associated with a common matrix C. This fact can be used to remove the relative permutation between \hat{C}_1 and \hat{C}_2 . Define

$$\rho_{k_1,k_2} = \frac{|(\hat{\boldsymbol{c}}_{1,k_1})^H \hat{\boldsymbol{c}}_{2,k_2}|}{\|\hat{\boldsymbol{c}}_{1,k_1}\|_2 \|\hat{\boldsymbol{c}}_{2,k_2}\|_2}$$
(48)

where \hat{c}_{1,k_1} and \hat{c}_{2,k_2} are, respectively, the k_1 th and k_2 th column of \hat{C}_1 and \hat{C}_2 . Since C has distinctive columns, with each column characterized by a different time delay parameter, ρ_{k_1,k_2} achieves the largest value when \hat{c}_{1,k_1} and \hat{c}_{2,k_2} correspond to the same target. Define a permutation matrix $\Pi_3 \triangleq [e_{\pi(1)} \cdots e_{\pi(K)}]^T \in \{0,1\}^{K \times K}$, where $e_{\pi(k)}$ is a standard basis vector, and $\pi(k) = \arg\max_{k_2} \{\rho_{k,k_2}\}_{k_2=1}^K$. Ignoring estimation errors, we should have

$$\Pi_2 = \Pi_1 \Pi_3 \tag{49}$$

Then we can utilize Π_3 to remove the permutation between $\{\hat{A}_1\}$ and $\{\hat{A}_2\}$, $\{\hat{B}_1\}$ and $\{\hat{B}_2\}$, $\{\hat{C}_1\}$ and $\{\hat{C}_2\}$. Specifically, defining $\tilde{A}_1 \triangleq \hat{A}_1\Pi_3$, $\tilde{B}_1 \triangleq \hat{B}_1\Pi_3$, $\tilde{C}_1 \triangleq \hat{C}_1\Pi_3$, we have

$$\tilde{A}_1 = A_1 \Lambda_1 \Pi_1 \Pi_3 + E_1 \Pi_3 = A_1 \Lambda_1 \Pi_2 + E_1 \Pi_3$$
 (50)

$$\tilde{B}_1 = B_1 \Lambda_2 \Pi_1 \Pi_3 + E_2 \Pi_3 = B_1 \Lambda_2 \Pi_2 + E_2 \Pi_3$$
 (51)

$$\tilde{C}_1 = C\Lambda_3\Pi_1\Pi_3 + E_3\Pi_3 = C\Lambda_3\Pi_2 + E_3\Pi_3$$
 (52)

Ignoring the permutation matrix Π_2 , we obtain

$$\begin{cases} \tilde{A}_1 = A_1 \Lambda_1 + E_1 \Pi_3 \\ \hat{A}_2 = A_2 \Gamma_1 + \tilde{E}_1 \end{cases}$$
 (53)

$$\begin{cases}
\tilde{B}_1 = B_1 \Lambda_2 + E_2 \Pi_3 \\
\hat{B}_2 = B_2 \Gamma_2 + \tilde{E}_2
\end{cases}$$
(54)

and

$$\begin{cases} \tilde{C}_1 = C\Lambda_3 + E_3\Pi_3 \\ \hat{C}_2 = C\Gamma_3 + \tilde{E}_3 \end{cases}$$
 (55)

Now we have column-aligned \tilde{A}_1 and \hat{A}_2 , \tilde{B}_1 and \hat{B}_2 , \tilde{C}_1 and \hat{C}_2 , i.e., the same columns of each pair of two factor matrices are associated with the same target. Note that both \tilde{C}_1 and \hat{C}_2 are estimated as a Vandermonde matrix based on the estimated generators. Hence theoretically we should have $\Gamma_3\Lambda_3^{-1}=I$.

C. Joint DOA, Time Delay and Doppler Estimation

Based on the column-aligned factor matrices from two phases, we discuss how to jointly estimate DOA, time delay and Doppler shift. Since $B_i = G^T \Phi_i \Xi$, and $G = \sigma u v^T$, (54) can be rewritten as

$$\begin{cases} \tilde{B}_1 = \sigma v u^T \Phi_1 \Xi \Lambda_2 + E_2 \Pi_3 \\ \hat{B}_2 = \sigma v u^T \Phi_2 \Xi \Gamma_2 + \tilde{E}_2 \end{cases}$$
 (56)

Also, (53) can be rewritten as

$$\begin{cases} \tilde{\mathbf{A}}_1 = \sigma \mathbf{W}^T \mathbf{v} \mathbf{u}^T \mathbf{\Phi}_1 \mathbf{\Xi} \mathbf{\Lambda}_1 \circledast \mathbf{D} + \mathbf{E}_1 \mathbf{\Pi}_3 \\ \hat{\mathbf{A}}_2 = \sigma \mathbf{W}^T \mathbf{v} \mathbf{u}^T \mathbf{\Phi}_2 \mathbf{\Xi} \mathbf{\Gamma}_1 \circledast \mathbf{D} + \tilde{\mathbf{E}}_1 \end{cases}$$
(57)

where $D \triangleq [d(\nu_1) \cdots d(\nu_K)] \in \mathbb{C}^{P \times K}$. Note both $\{A_i\}$ and $\{B_i\}$ contain the DOA information. To harness the IRS illumination diversity across two phases, we define a new vector $\hat{r}_k^B \in \mathbb{C}^M$, in which the mth entry is calculated by the elementwise division of $[\tilde{B}_1]_{m,k}$ and $[\hat{B}_2]_{m,k}$, i.e.,

$$[\hat{\boldsymbol{r}}_{k}^{B}]_{m} \triangleq \frac{[\tilde{\boldsymbol{B}}_{1}]_{m,k}}{[\hat{\boldsymbol{B}}_{2}]_{m,k}}$$

$$= \frac{\sigma[\boldsymbol{v}]_{m}\boldsymbol{u}^{T}\boldsymbol{\Phi}_{1}\boldsymbol{a}(\theta_{k})[\boldsymbol{\Lambda}_{2}]_{k,k}}{\sigma[\boldsymbol{v}]_{m}\boldsymbol{u}^{T}\boldsymbol{\Phi}_{2}\boldsymbol{a}(\theta_{k})[\boldsymbol{\Gamma}_{2}]_{k,k}} + \epsilon_{m,k}$$

$$= \frac{\boldsymbol{u}^{T}\boldsymbol{\Phi}_{1}\boldsymbol{a}(\theta_{k})[\boldsymbol{\Lambda}_{2}]_{k,k}}{\boldsymbol{u}^{T}\boldsymbol{\Phi}_{2}\boldsymbol{a}(\theta_{k})[\boldsymbol{\Gamma}_{2}]_{k,k}} + \epsilon_{m,k}$$
(58)

Similarly, define $\hat{\boldsymbol{r}}_k^A \in \mathbb{C}^P$, we have

$$[\hat{\boldsymbol{r}}_{k}^{A}]_{p} \triangleq \frac{[\tilde{\boldsymbol{A}}_{1}]_{p,k}}{[\hat{\boldsymbol{A}}_{2}]_{p,k}}$$

$$= \frac{\sigma \boldsymbol{w}_{p}^{T} \boldsymbol{v} \boldsymbol{u}^{T} \boldsymbol{\Phi}_{1} \boldsymbol{a}(\boldsymbol{\theta}_{k}) [\boldsymbol{\Lambda}_{1}]_{k,k}}{\sigma \boldsymbol{w}_{p}^{T} \boldsymbol{v} \boldsymbol{u}^{T} \boldsymbol{\Phi}_{2} \boldsymbol{a}(\boldsymbol{\theta}_{k}) [\boldsymbol{\Gamma}_{1}]_{k,k}} + \varepsilon_{p,k}$$

$$= \frac{\boldsymbol{u}^{T} \boldsymbol{\Phi}_{1} \boldsymbol{a}(\boldsymbol{\theta}_{k}) [\boldsymbol{\Lambda}_{1}]_{k,k}}{\boldsymbol{u}^{T} \boldsymbol{\Phi}_{2} \boldsymbol{a}(\boldsymbol{\theta}_{k}) [\boldsymbol{\Gamma}_{1}]_{k,k}} + \varepsilon_{p,k}$$
(59)

where w_p denotes the pth column of W, both $\epsilon_{m,k}$ and $\varepsilon_{p,k}$ are noise terms. We now discuss how to recover the DOA parameter from (58) and (59). Define

$$\hat{\gamma}(\theta_k) \triangleq \frac{1}{M} \sum_{m=1}^{M} [\hat{\boldsymbol{r}}_k^B]_m \cdot \frac{1}{P} \sum_{m=1}^{P} [\hat{\boldsymbol{r}}_k^A]_p$$
 (60)

Ignoring the noise term, $\hat{\gamma}(\theta_k)$ is equivalent to

$$\hat{\gamma}(\theta_{k}) = \frac{\boldsymbol{u}^{T} \boldsymbol{\Phi}_{1} \boldsymbol{a}(\theta_{k}) [\boldsymbol{\Lambda}_{2}]_{k,k}}{\boldsymbol{u}^{T} \boldsymbol{\Phi}_{2} \boldsymbol{a}(\theta_{k}) [\boldsymbol{\Gamma}_{2}]_{k,k}} \cdot \frac{\boldsymbol{u}^{T} \boldsymbol{\Phi}_{1} \boldsymbol{a}(\theta_{k}) [\boldsymbol{\Lambda}_{1}]_{k,k}}{\boldsymbol{u}^{T} \boldsymbol{\Phi}_{2} \boldsymbol{a}(\theta_{k}) [\boldsymbol{\Gamma}_{1}]_{k,k}}$$

$$= \left(\frac{\boldsymbol{u}^{T} \boldsymbol{\Phi}_{1} \boldsymbol{a}(\theta_{k})}{\boldsymbol{u}^{T} \boldsymbol{\Phi}_{2} \boldsymbol{a}(\theta_{k})}\right)^{2} [\boldsymbol{\Lambda}_{2}]_{k,k} [\boldsymbol{\Gamma}_{2}]_{k,k}^{-1} [\boldsymbol{\Lambda}_{1}]_{k,k} [\boldsymbol{\Gamma}_{1}]_{k,k}^{-1}$$

$$= \left(\frac{\boldsymbol{u}^{T} \boldsymbol{\Phi}_{1} \boldsymbol{a}(\theta_{k})}{\boldsymbol{u}^{T} \boldsymbol{\Phi}_{2} \boldsymbol{a}(\theta_{k})}\right)^{2} [\boldsymbol{\Gamma}_{3}]_{k,k} [\boldsymbol{\Lambda}_{3}]_{k,k}^{-1}$$

$$\stackrel{(a)}{=} \left(\frac{\boldsymbol{u}^{T} \boldsymbol{\Phi}_{1} \boldsymbol{a}(\theta_{k})}{\boldsymbol{u}^{T} \boldsymbol{\Phi}_{2} \boldsymbol{a}(\theta_{k})}\right)^{2}$$

$$\stackrel{(b)}{=} (\boldsymbol{a})$$

$$\stackrel{(a)}{=} \left(\frac{\boldsymbol{u}^{T} \boldsymbol{\Phi}_{1} \boldsymbol{a}(\theta_{k})}{\boldsymbol{u}^{T} \boldsymbol{\Phi}_{2} \boldsymbol{a}(\theta_{k})}\right)^{2}$$

$$\stackrel{(b)}{=} (\boldsymbol{a})$$

where (a) comes from the fact that $\Lambda_1 \Lambda_2 \Lambda_3 = I$, $\Gamma_1 \Gamma_2 \Gamma_3 = I$, and $[\Gamma_3]_{k,k} [\Lambda_3]_{k,k}^{-1} = 1$. As for now, we see that the scaling ambiguities in (58) and (59) are effectively removed and an unambiguous estimate of θ can be obtained.

Based on the above relationship (61), we can estimate the target's DOA via the following criterion

$$\hat{\theta}_{k} = \underset{\theta}{\operatorname{arg\,min}} \quad \|\hat{\gamma}(\theta_{k}) - \gamma(\theta)\|_{2}^{2}$$
s.t.
$$\gamma(\theta) = \left(\frac{\boldsymbol{u}^{T}\boldsymbol{\Phi}_{1}\boldsymbol{a}(\theta)}{\boldsymbol{u}^{T}\boldsymbol{\Phi}_{2}\boldsymbol{a}(\theta)}\right)^{2}$$

$$\theta \in \mathcal{D}_{\theta}$$
 (62)

where \mathcal{D}_{θ} is the feasible region of θ and the above problem can be easily solved by a one-dimensional search.

Note that the kth column of A_i is characterized by both θ_k and ν_k . Specifically, the kth column of A_i and the kth column of B_i are related as

$$\boldsymbol{z}_{i}(\theta_{k}, \nu_{k}) = (\boldsymbol{W}^{T} \boldsymbol{b}_{i}(\theta_{k})) \circledast (\boldsymbol{d}(\nu_{k}))$$
(63)

After the DOA is estimated, define $\check{\boldsymbol{B}}_i = \boldsymbol{G}^T \boldsymbol{\Phi}_i \hat{\boldsymbol{\Xi}} \in \mathbb{C}^{M \times K}$ with $\hat{\boldsymbol{\Xi}} \triangleq [\boldsymbol{a}(\hat{\theta}_1) \cdots \boldsymbol{a}(\hat{\theta}_K)]$, and define $\check{\boldsymbol{A}}_i \in \mathbb{C}^{P \times K}$ with $[\check{\boldsymbol{A}}_1]_{p,k} = [\check{\boldsymbol{A}}_1]_{p,k}/[\boldsymbol{W}^T \check{\boldsymbol{B}}_1]_{p,k}, [\check{\boldsymbol{A}}_2]_{p,k} = [\hat{\boldsymbol{A}}_2]_{p,k}/[\boldsymbol{W}^T \check{\boldsymbol{B}}_2]_{p,k}.$ Note that each column of $\check{\boldsymbol{A}}_i$ is characterized by the associated Doppler shift ν_k . Hence, the Doppler shift ν_k can be estimated via a correlation-based scheme [41] as

$$\hat{\nu}_{i,k} = \underset{\nu_k}{\operatorname{arg\,max}} \frac{|\check{\boldsymbol{a}}_{i,k}^H \boldsymbol{d}(\nu_k)|}{\|\check{\boldsymbol{a}}_{i,k}\|_2 \|\boldsymbol{d}(\nu_k)\|_2}$$
(64)

where $\check{a}_{i,k}$ denotes the kth column of \check{A}_i . We then compute the average of the two estimates as the final estimate of the Doppler shift, i.e., $\hat{\nu}_k = (\hat{\nu}_{1,k} + \hat{\nu}_{2,k})/2$. The velocity estimate of the kth target can be calculated as $\hat{v}_k = \hat{\nu}_k c/2f_c$. The round-trip time delay $\{\hat{\tau}_{i,k}\}$ can be calculated from the estimated generators $\{\hat{t}_{i,k}\}$ in (41) as

$$\hat{\tau}_{i,k} = \frac{\arg(\hat{t}_{i,k})}{-2\pi\Delta f} \tag{65}$$

where $\arg(\hat{t}_{i,k})$ denotes the argument of the complex number $\hat{t}_{i,k}$. Similarly, we obtain $\hat{\tau}_k = (\hat{\tau}_{1,k} + \hat{\tau}_{2,k})/2$.

V. CRB ANALYSIS

In this section, we provide a CRB analysis of the estimation problem considered in this paper. For the $P \times M \times L$ tensor observation \mathbf{y}_i considered in (22), we have

$$\mathbf{\mathcal{Y}}_{i} = \sum_{k=1}^{K} \mathbf{z}_{i}(\theta_{k}, \nu_{k}) \circ \mathbf{b}_{i}(\theta_{k}) \circ \alpha_{k} \mathbf{f}(\tau_{k}) + \mathbf{\mathcal{N}}_{i}$$
 (66)

We write the unknown target parameters as

$$\boldsymbol{\zeta} = [\boldsymbol{\theta}^T \ \boldsymbol{\nu}^T \ \boldsymbol{\tau}^T] \in \mathbb{R}^{1 \times 3K}$$
 (67)

(61) where $\boldsymbol{\theta} \triangleq [\theta_1 \cdots \theta_K]^T$, $\boldsymbol{\nu} \triangleq [\nu_1 \cdots \nu_K]^T$ and $\boldsymbol{\tau} \triangleq [\tau_1 \cdots \tau_K]^T$. The log-likelihood function of the parameter

vector ζ can be expressed as

$$\mathcal{L}(\zeta) = \sum_{i=1}^{2} -\tilde{D}_{i} - \frac{1}{\sigma_{i}^{2}} \| \mathbf{\mathcal{Y}}_{i,(1)} - \mathbf{A}_{i} (\mathbf{C} \odot \mathbf{B}_{i})^{T} \|_{F}^{2}$$

$$= \sum_{i=1}^{2} -\tilde{D}_{i} - \frac{1}{\sigma_{i}^{2}} \| \mathbf{\mathcal{Y}}_{i,(2)} - \mathbf{B}_{i} (\mathbf{C} \odot \mathbf{A}_{i})^{T} \|_{F}^{2}$$

$$= \sum_{i=1}^{2} -\tilde{D}_{i} - \frac{1}{\sigma_{i}^{2}} \| \mathbf{\mathcal{Y}}_{i,(3)} - \mathbf{C} (\mathbf{B}_{i} \odot \mathbf{A}_{i})^{T} \|_{F}^{2}$$
(68)

where $\tilde{D}_i \triangleq PML \ln(\pi \sigma_i^2)$, and $\mathcal{Y}_{i,(j)}$ denotes the mode-j unfolding of \mathcal{Y}_i . Then the fisher information matrix (FIM) for ζ is given by

$$\Omega(\zeta) = \mathbb{E}\left\{ \left(\frac{\partial \mathcal{L}(\zeta)}{\partial \zeta} \right)^{H} \left(\frac{\partial \mathcal{L}(\zeta)}{\partial \zeta} \right) \right\}$$
(69)

To calculate $\Omega(\zeta)$, we first compute the partial derivative of $\mathcal{L}(\zeta)$ with respect to ζ and then calculate its expectation.

A. Partial Derivative of $\mathcal{L}(\zeta)$

Following a similar procedure as in [41], [42], the partial derivative of $\mathcal{L}(\zeta)$ w.r.t. θ_k can be calculated as

$$\frac{\partial \mathcal{L}(\zeta)}{\partial \theta_{k}} = \sum_{i=1}^{2} \frac{2}{\sigma_{i}^{2}} \Re \left\{ \boldsymbol{e}_{k}^{T} \left(\boldsymbol{C} \odot \boldsymbol{B}_{i} \right)^{T} \times \left(\boldsymbol{\mathcal{Y}}_{i,(1)} - \boldsymbol{A}_{i} \left(\boldsymbol{C} \odot \boldsymbol{B}_{i} \right)^{T} \right)^{H} \boldsymbol{A}_{i,\theta}^{\prime} \boldsymbol{e}_{k} \right\}
+ \sum_{i=1}^{2} \frac{2}{\sigma_{i}^{2}} \Re \left\{ \boldsymbol{e}_{k}^{T} \left(\boldsymbol{C} \odot \boldsymbol{A}_{i} \right)^{T} \times \left(\boldsymbol{\mathcal{Y}}_{i,(2)} - \boldsymbol{B}_{i} \left(\boldsymbol{C} \odot \boldsymbol{A}_{i} \right)^{T} \right)^{H} \boldsymbol{B}_{i,\theta}^{\prime} \boldsymbol{e}_{k} \right\}$$
(70)

in which $A'_{i,\theta} \triangleq [a'_{i,\theta_1} \cdots a'_{i,\theta_K}] \in \mathbb{C}^{P \times K}$ and $B'_{i,\theta} \triangleq [b'_{i,\theta_1} \cdots b'_{i,\theta_K}] \in \mathbb{C}^{M \times K}$, with $a'_{i,\theta_k} \triangleq \frac{\partial [A_i]_{:,k}}{\partial \theta_k}$ and $b'_{i,\theta_k} \triangleq \frac{\partial [B_i]_{:,k}}{\partial \theta_k}$. e_k is a standard basis vector with k as the index of its nonzero element. Similarly, the partial derivatives w.r.t. other parameters can be calculated. The details are omitted here for brevity.

B. Calculation of FIM $\Omega(\zeta)$

To calculate the FIM $\Omega(\zeta)$, we first calculate the entries in the diagonal blocks. Define $u=K(k_1-1)+k_1$ and $v=K(k_2-1)+k_2$. The (k_1,k_2) th element in the block related to θ , can be calculated as

$$\mathbb{E}\left\{ \left(\frac{\partial \mathcal{L}(\zeta)}{\partial \theta_{k_1}} \right)^* \left(\frac{\partial \mathcal{L}(\zeta)}{\partial \theta_{k_2}} \right) \right\}$$

$$= 2\Re\{ [\boldsymbol{C}_{\boldsymbol{n}_{A,\theta}}]_{u,v} \} + 2\Re\{ [\boldsymbol{C}_{\boldsymbol{n}_{A_{\theta},B}}]_{u,v} \}$$

$$+ 2\Re\{ [\boldsymbol{C}_{\boldsymbol{n}_{B,A_{\theta}}}]_{u,v} \} + 2\Re\{ [\boldsymbol{C}_{\boldsymbol{n}_{B,\theta}}]_{u,v} \}$$
(71)

where

$$C_{n_{A,\theta}} = \sum_{i=1}^{2} \frac{2}{\sigma_{i}^{2}} \left(A'_{i,\theta} \otimes (C \odot B_{i}) \right)^{T} \times \left(A'_{i,\theta} \otimes (C \odot B_{i}) \right)^{*}$$
(72)

$$C_{n_{A_{\theta},B}} = \sum_{i=1}^{2} \frac{1}{\sigma_{i}^{4}} \left(\mathbf{A}'_{i,\theta} \otimes (\mathbf{C} \odot \mathbf{B}_{i}) \right)^{T} C_{1,2}^{i} \times \left(\mathbf{B}'_{i,\theta} \otimes (\mathbf{C} \odot \mathbf{A}_{i}) \right)^{*}$$
(73)

$$C_{n_{B,A_{\theta}}} = \sum_{i=1}^{2} \frac{1}{\sigma_{i}^{4}} \left(\mathbf{B}'_{i,\theta} \otimes (\mathbf{C} \odot \mathbf{A}_{i}) \right)^{T} C_{2,1}^{i} \times \left(\mathbf{A}'_{i,\theta} \otimes (\mathbf{C} \odot \mathbf{B}_{i}) \right)^{*}$$
(74)

$$C_{n_{B,\theta}} = \sum_{i=1}^{2} \frac{1}{\sigma_{i}^{2}} \left(B'_{i,\theta} \otimes (C \odot A_{i}) \right)^{T} \times \left(B'_{i,\theta} \otimes (C \odot A_{i}) \right)^{*}$$
(75)

and

$$\boldsymbol{C}_{j_1,j_2}^i \triangleq \mathbb{E}\{\operatorname{vec}(\boldsymbol{\mathcal{N}}_{i,(j_1)}^H)\operatorname{vec}(\boldsymbol{\mathcal{N}}_{i,(j_2)}^H)^H\}$$
 (76)

in which i is phase index and the details will be discussed later. Similarly, the entries in other blocks can be derived The details are omitted due to space limit.

Now we compute $C^i_{j_1,j_2}$ defined in (76). Note the entries in \mathcal{N}_i are all i.i.d Gaussian random variables, we have

$$\mathbb{E}\{n_{i,p_1,m_1,l_1}n_{i,p_2,m_2,l_2}^*\} = \begin{cases} \sigma_i^2, & p_1 = p_2, m_1 = m_2, l_1 = l_2\\ 0, & \text{otherwise} \end{cases}$$
(77)

Based on the arrangements of elements of \mathcal{N}_i under different unfolding modes, the PML nonzero entries in $C^i_{j_1,j_2} \in \mathbb{C}^{PML \times PML}$ can be given as

$$[C_{j_1,j_2}^i]_{u,v} = \begin{cases} \sigma_i^2, & u = h_{j_1}(p,m,l), v = h_{j_2}(p,m,l) \\ 0, & \text{otherwise} \end{cases}$$
(78)

where $\forall j_1 \neq j_2, 1 \leq j_1 \leq 3, 1 \leq j_2 \leq 3$, and

$$hbar_1(p, m, l) = m + (l - 1)M + (p - 1)ML$$
(79)

$$h_2(p, m, l) = p + (l - 1)P + (m - 1)PL$$
 (80)

$$h_3(p, m, l) = p + (m - 1)P + (l - 1)PM$$
 (81)

After obtaining the FIM Ω , the CRB can be calculated as

$$CRB(\zeta) = \Omega^{-1}(\zeta) \tag{82}$$

From our CRB analysis, we can see that the sensing performance is dependent on a number of factors, including the number of pulses P, the number of subcarriers L, the number of AP's antennas M, as well as the signal-to-noise ratio (SNR). From the numerical calculation of the CRB results, we know that increasing these parameters leads to a better sensing performance, which is expected and can be intuitively explained. Specifically, increasing the number of pulses P provides a larger observation window for the Doppler shift, which in turn helps enhance the Doppler shift estimation accuracy. Similarly, increasing the number of subcarriers L renders more observations about the time delay and can thus improve the time delay estimation performance.

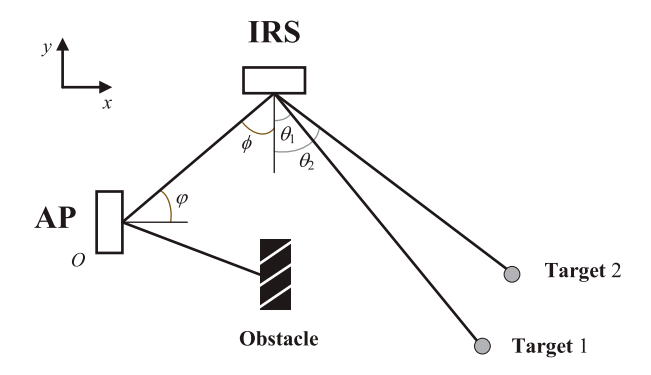


Fig. 5. Simulation setup (top view).

VI. SIMULATION RESULTS

We now present numerical results to evaluate the estimation performance of the proposed method for NLOS target sensing. We examine a two-dimensional scenario, as illustrated in Fig. 5, where the AP and the IRS are located at coordinates $p_{
m AP}$ = $[0,0]^T$ and $p_{IRS} = [100,100]^T$ m, respectively. In our simulations, the system carrier frequency is set to $f_c = 60$ GHz, and the distance between two adjacent antenna elements d is set to half of the signal wavelength. The number of antennas at the AP and the number of reflecting elements at the IRS are set to M=16 and N=32, respectively. For OFDM signals, the subcarrier spacing is set to $\Delta f = 500 \text{kHz}$. As a result, the length of an effective OFDM symbol is equal to $T_d = \frac{1}{\Delta f} = 2 \,\mu s$, and the length of the CP is set to $T_{\rm cp}=1~\mu {\rm s}$ [32]. The bandwidth of the OFDM signal can be calculated as $L\Delta f$, where L denotes the number of subcarriers and its choice will be specified later. The pulse repetition interval is set to $T_{PRI} = 8 \,\mu s$. The channel of the AP-IRS link is generated based on the geometric channel model and includes only a LOS path, i.e.

$$G = \rho a_{\rm IRS}(\phi) a_{\rm AP}^H(\varphi) \tag{83}$$

where ρ denotes the path loss between the AP and the IRS, ϕ and φ denote the angle of arrival (AOA) and angle of departure (AOD), respectively. The distance-dependent path loss γ follows a complex normal distribution $\mathcal{CN}(0, 10^{-0.1\kappa})$, where $\kappa =$ $a + 10b \log_{10}(D) + \xi$. Here, $\xi \sim \mathcal{N}(0, \sigma_{\xi}^2)$, and D represents the distance between the the AP and the IRS. The parameters a, b, and σ_{ξ} are set to a = 68, b = 2, and $\sigma_{\xi} = 5.8$ dB, as suggested in [43], [44]. In our experiments, we consider K=2targets, both located within the angular range of $[30^{\circ}, 45^{\circ}]$ with respect to the IRS. The coordinates of the targets are set as $\boldsymbol{p}_1 = [533, -170]^T$ m and $\boldsymbol{p}_2 = [541, -245]^T$ m. The targets radial velocities with respect to the IRS are set to $v_1 = 16.66$ m/s and $v_2 = -22$ m/s, respectively. The direct link between the AP and the targets are blocked by obstacles. So the AP has to detect these two targets via the IRS-assisted reflected path. The radar cross-section (RCS) of each target is set to 1 for simplicity, as suggested by [22].

In our experiments, the beamforming vector \mathbf{w}_p is designed to align its beam direction towards the IRS to maximize the received signal power at the IRS. The IRS phase shift profiles are

generated according to the method discussed in Section. Specifically, we partition the IRS into 4 subarrays, and the pointing directions of these 4 subarrays are set to $\{30^\circ, 35^\circ, 40^\circ, 45^\circ\}$ for phase 1 and $\{48^\circ, 42^\circ, 36^\circ, 30^\circ\}$ for phase 2. This scheme allows the IRS to generating directional beams to effectively illuminate the potential target area, meanwhile exhibiting diverse illumination patterns across different phases.

Unless otherwise stated, the numbers of subcarriers and pulses, as well as the transmit power, are set to L=10, P=10, and $P_t=30\,$ dBm, respectively. The received signal-to-noise ratio (SNR) is defined as

$$SNR \triangleq \frac{\|\mathcal{Y} - \mathcal{N}\|_F^2}{\|\mathcal{N}\|_F^2}$$
 (84)

where \mathcal{Y} and \mathcal{N} represent the received signal and the additive noise in (22), respectively. All results are averaged over 10^3 Monte Carlo runs.

A. Performance Evaluation of the Proposed Method

We first examine the performance of our proposed method in estimating the target's parameters $\{\theta_k, \tau_k, \nu_k\}$. The performance is evaluated by the mean square error (MSE), which is defined as

$$MSE(\zeta) = \frac{1}{K} \sum_{k=1}^{K} \mathbb{E}\left(\|\zeta_k - \hat{\zeta}_k\|_2^2\right)$$
 (85)

where ζ denotes an estimate of the parameter ζ , which corresponds to one of the parameters $\{\theta, \tau, \nu\}$. The MSE of our proposed method as a function of the SNR is plotted in Fig. 6(a)– 6(c). The CRB results for different sets of parameters are also included for comparison. From Fig. 6, we see that as the SNR increases, our proposed method achieves an estimation accuracy that is close to the theoretical lower bound. This result validates the efficiency of the proposed method for NLOS target sensing. Specifically, the MSE of the DOA is able to approach its CRB. The estimate of the other two parameters (Doppler shift and delay) cannot exactly attain their respective CRBs, which is probably because the observation time/signal bandwidth is not long/large enough to estimate these two parameters. Additionally, from Fig. 6, it is seen that the proposed method provides accurate estimates of the target's parameters even in a relatively low SNR regime, say SNR = -5 dB. Notably, for NLOS sensing tasks, the SNR is usually low due to the roundtrip path loss and reflection loss. Hence the ability of extracting parameters reliably under a low SNR environment has a significant implication in practice.

Next, we plot the MSEs of the proposed method as a function of the number of pulses P in Fig. 7(a)–7(c), where the number of subcarriers is set to L=10, and the SNR is set to 5 dB. We see that the proposed method can achieve reliable sensing even with a small number of pulses, for example, P=5, which corresponds to a total sensing duration of $(2P+1)T_{\rm PRI}=88~\mu \rm s$. This result corroborates the efficiency of the proposed method for NLOS sensing tasks.

In Fig. 8(a)–8(c), we depict the estimation performance of the proposed method as a function of the number of subcarriers,

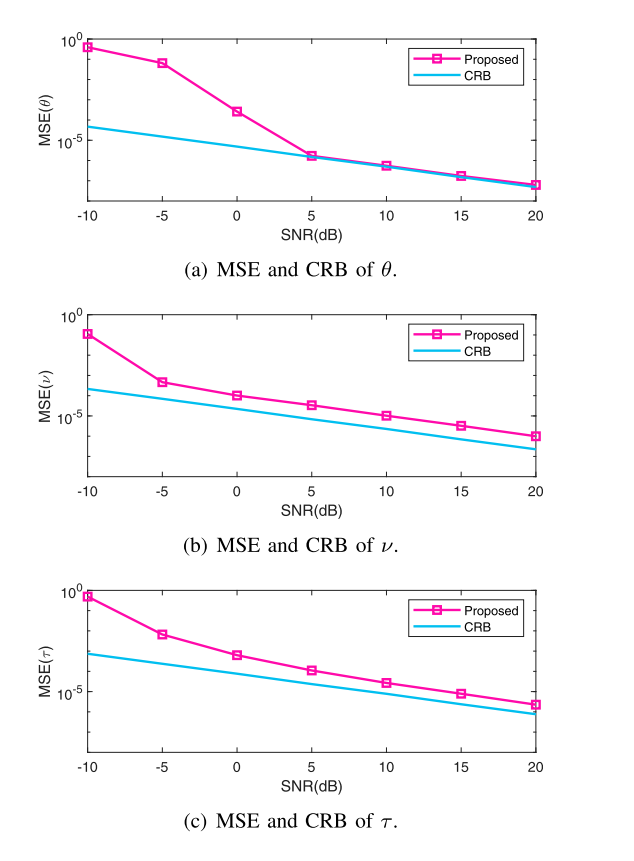


Fig. 6. MSEs and CRBs versus SNR.

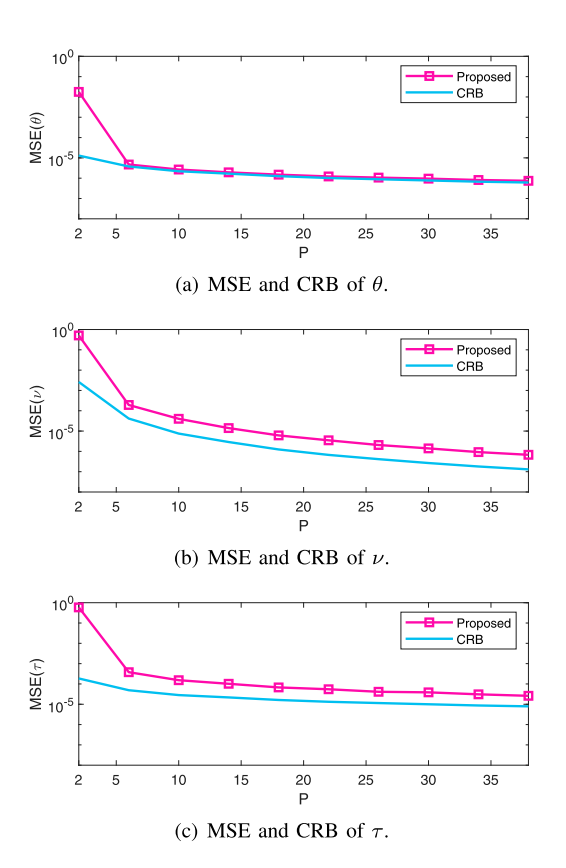


Fig. 7. MSEs and CRBs versus the number of pulses.

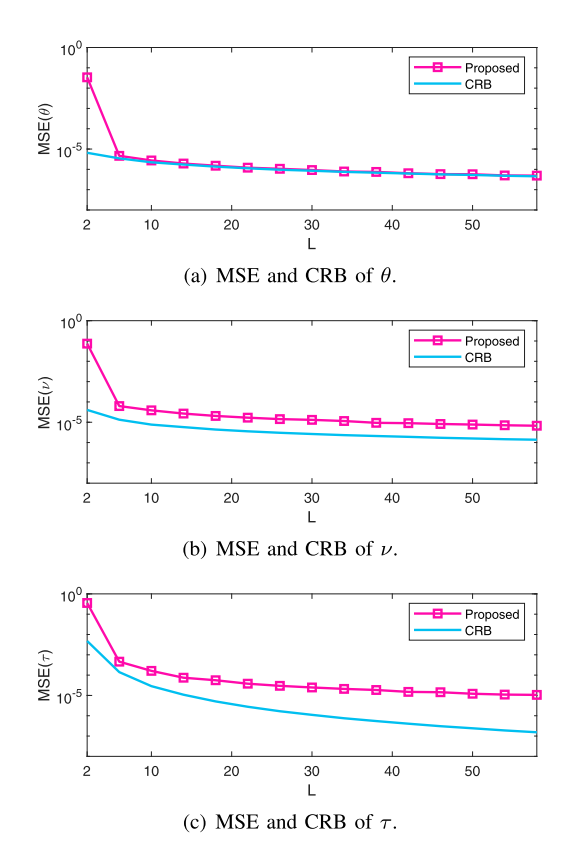


Fig. 8. MSEs and CRBs versus the number of subcarriers.

where the number of pulses is set to P=10 and the SNR is set to 5 dB. The results show that our proposed method can deliver accurate estimates of the target's parameters even with a small number of subcarriers. We also observe that our proposed method fails when the number of subcarriers $L \leq 2$. This is because, when P=10>K and M=16>K, the uniqueness condition (31) is satisfied only when $(L-1)\geq 1$, implying that $L\geq 2$. Hence, the results roughly coincide with our analysis concerning the uniqueness of the CP decomposition.

In Fig. 9(a)–9(c), we plot the estimation performance of the proposed method versus the number of AP's antennas. In this experiment, the number of subcarriers and the number of pulses are set to L=8 and P=8, respectively. The SNR is fixed at 5 dB. As expected, the estimation performance improves with an increasing number of antennas M. Furthermore, it is observed that the proposed method can deliver decent performance even with a few number of antennas employed at the AP. This result also corroborates well with our analysis concerning the uniqueness condition of the CP decomposition.

B. Imperfect AP-IRS Channel Knowledge

Next, we examine the performance of our proposed method when we only have an imperfect knowledge of the AP-IRS channel G. Specifically, we use the statistical CSI error model [45], [46] to characterize the channel inaccuracies:

$$G = \hat{G} + \Delta G \tag{86}$$

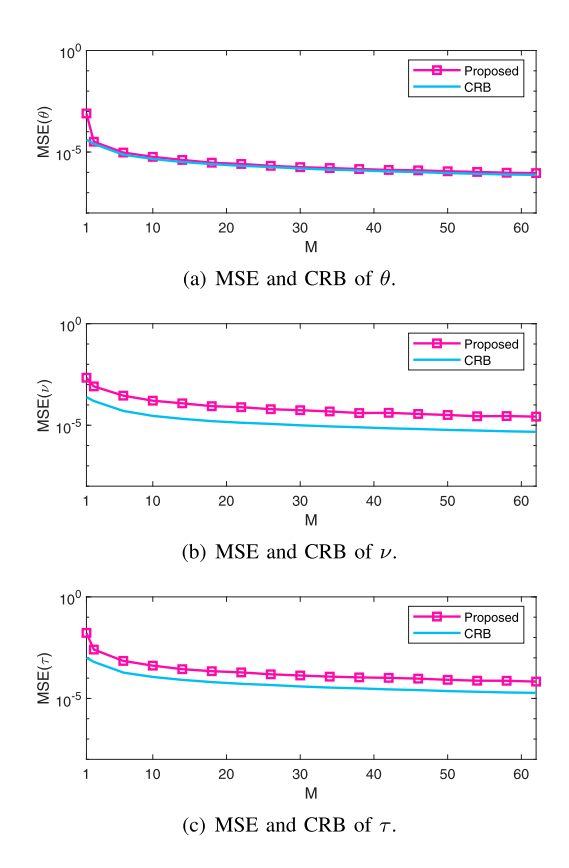


Fig. 9. MSEs and CRBs versus the number of AP's antennas.

where \hat{G} denotes the estimated AP-IRS channel, and ΔG denotes the estimation error whose entries follow a circularly symmetric complex Gaussian (CSCG) distribution, i.e.,

$$\operatorname{vec}(\Delta \mathbf{G}) \sim \mathcal{CN}(0, \Sigma_g), \quad \Sigma_g \succeq 0$$
 (87)

where $\Sigma_g = \varepsilon_g^2 \mathbf{I}_{MN} \in \mathbb{C}^{MN \times MN}.$ In our experiments, the variance of $\text{vec}(\Delta G)$ is defined as $\varepsilon_g^2 = \delta_g^2 \|\text{vec}(\hat{G})\|_2^2$, where $\delta_a \in [0,1)$ measures the CSI uncertainty [45]. Fig. 10 shows the estimation performance of the proposed method versus SNR under different levels of channel uncertainty. It can be observed that our proposed algorithm exhibits robust performance even when the CSI of the AP-IRS channel is imperfect. Additionally, from the results we see that the DOA estimation performance degrades as the channel uncertainty increases, whereas the channel uncertainty has little effect on the Doppler shift and time delay estimation performance. The reason can be explained as follows. First, the time delay is calculated from the estimated generators based on equations (41) and (65), which are independent of the AP-IRS channel. Moreover, the Doppler shift estimation benefits from the Hadamard product structure in (25), which preserves the steering vector structure of ν , making the Doppler shift estimation robust to variations in G.

C. Performance Comparison With The Existing Method [22]

To illustrate the superiority of the proposed method, we compare it with the MLE-based method [22]. For a fair comparison,

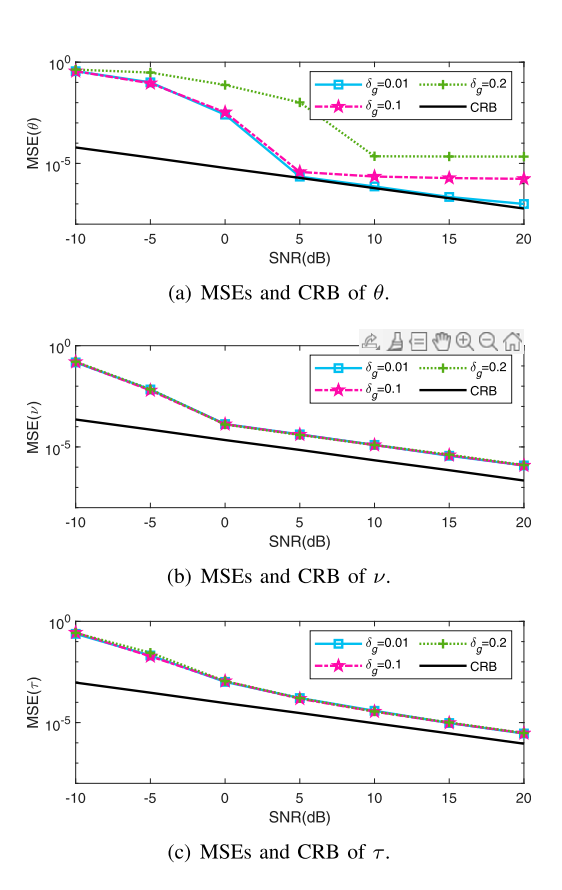


Fig. 10. MSEs and CRBs versus SNR under different levels of channel uncertainty.

the AP-IRS channel is assumed to be Rician fading in our simulations, i.e.

$$G = \sqrt{\frac{\gamma}{1+\gamma}}G^{\text{LOS}} + \sqrt{\frac{1}{1+\gamma}}G^{\text{NLOS}}$$
 (88)

where γ is the Rician factor in dB while G^{LOS} and G^{NLOS} are the LOS and NLOS components, respectively. A typical value of the Rician factor over the millimeter-wave (mmWave) band is 13 dB [47], [48], [49], indicating that G is an approximately rank-one matrix. In our experiments, we also consider the cases where the Rician factor is set to 0 dB and 5 dB, in order to more comprehensively examine the performance of our proposed method under different channel conditions. Note that [22] employs a single-carrier signal to sense a single static target. In contrast, this paper aims to sense multiple moving targets based on the OFDM signal. To make a fair comparison, we focus our simulations on a single static target. The Doppler shift is set to $\nu = 0$ in (11). It is crucial to emphasize that our proposed method estimates not only the DOA but also the Doppler shift and the time delay, whereas [22] can only estimate the DOA. In our experiments, we assume there is one LOS path and four NLOS paths between the AP and the IRS, resulting in rank(G) = 5. Also, for a fair comparison, the number of measurements used for parameter estimation is set the same for both methods.

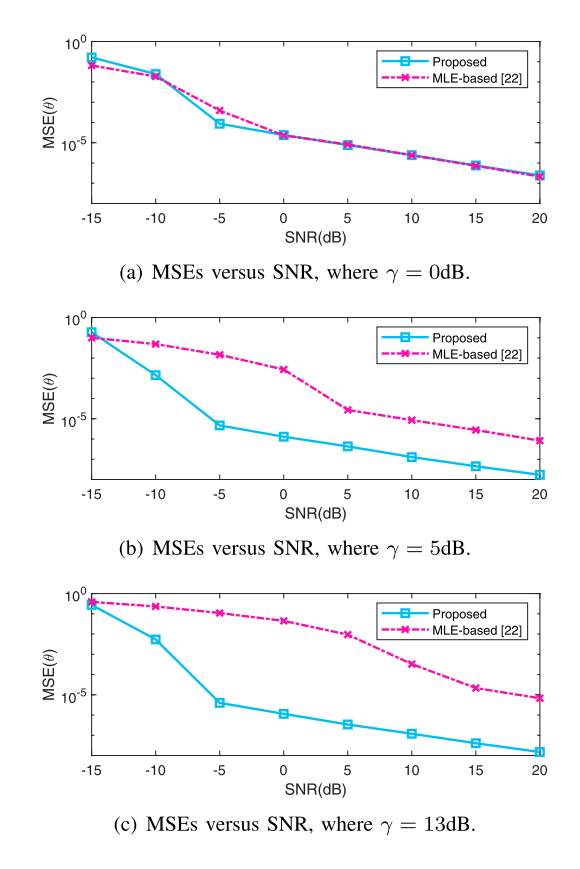


Fig. 11. MSEs achieved by respective algorithms versus SNR, where K=1 and $\mathrm{rank}({\bf G})=5$.

Fig. 11 depicts the MSE of the estimated DOA parameter as a function of the SNR under different Rician factor values. From Fig. 11(b) and Fig. 11(c), we observe that our proposed algorithm presents a clear performance advantage over the MLE method [22]. This performance improvement becomes more significant as the Rician factor increases. The reason for this observation can be explained as follows. The work [22] requires additional degrees-of-freedom provided by the AP-IRS channel in order to resolve the scaling ambiguity in the DOA estimation. However, as the Rician factor increases, the AP-IRS channel becomes an approximately rank-one matrix, yielding an insufficient degrees-of-freedom for DOA estimation. As a result, the method [22] incurs a significant amount of performance degradation as the Rician factor increases. In contrast to [22], our proposed method removes the scaling ambiguity of DOA estimation by leveraging the IRS illumination diversity across two phases. Therefore, it works well even for rank-one AP-IRS channel scenarios.

Note that our proposed algorithm can be readily adapted to the scenario where the BS-IRS channel has a rank greater than one. In fact, in such a case, a single tensor alone can identify the DOA parameter. Specifically, we can resort to (46) to estimate the DOA parameter when $\gamma=0$ dB. From Fig. 11, we see that our proposed method not only presents a significant performance improvement over the work [22] for approximately rank-one scenarios (corresponding to $\gamma=5$ dB and $\gamma=13$ dB), but

also achieves a performance close to the work [22] when the AP-IRS channel consists of multiple strong paths (corresponding to $\gamma=0\,\mathrm{dB}$).

VII. CONCLUSION

In this paper, we explored an IRS-assisted NLOS sensing system. We introduced a radar operation mode for the AP, which senses the NLOS environment by transmitting OFDM pulses and processing echoes relayed by the IRS. A two-phase sensing scheme was proposed by exploiting the diversity in the illumination pattern of the IRS across two different phases. Using this two-phase sensing approach, we developed a CP decomposition-based method for estimating the DOA, Doppler shifts, and time delays of the targets. Uniqueness conditions for the proposed method are analyzed and provided. We also conducted a CRB analysis for the considered estimation problem. Simulation results demonstrated the effectiveness of the proposed method in performing NLOS sensing, even in scenarios where there was only a single dominant path between the AP and the IRS.

REFERENCES

- [1] Q. Wu and R. Zhang, "Intelligent reflecting surface enhanced wireless network via joint active and passive beamforming," *IEEE Trans. Wireless Commun.*, vol. 18, no. 11, pp. 5394–5409, Nov. 2019.
- [2] M. Di Renzo et al., "Smart radio environments empowered by reconfigurable intelligent surfaces: How it works, state of research, and the road ahead," *IEEE J. Sel. Areas in Commun.*, vol. 38, no. 11, pp. 2450–2525, Nov. 2020.
- [3] Q. Wu and R. Zhang, "Towards smart and reconfigurable environment: Intelligent reflecting surface aided wireless network," *IEEE Commun. Mag.*, vol. 58, no. 1, pp. 106–112, Jan. 2020.
- [4] Q. Wu, S. Zhang, B. Zheng, C. You, and R. Zhang, "Intelligent reflecting surface-aided wireless communications: A tutorial," *IEEE Trans. Commun.*, vol. 69, no. 5, pp. 3313–3351, May 2021.
- [5] P. Wang, J. Fang, X. Yuan, Z. Chen, and H. Li, "Intelligent reflecting surface-assisted millimeter wave communications: Joint active and passive precoding design," *IEEE Trans. Veh. Technol.*, vol. 69, no. 12, pp. 14960–14973, Dec. 2020.
- [6] P. Wang, J. Fang, L. Dai, and H. Li, "Joint transceiver and large intelligent surface design for massive MIMO mmWave systems," *IEEE Trans. Wireless Commun.*, vol. 20, no. 2, pp. 1052–1064, Feb. 2021.
- [7] B. Ning, P. Wang, L. Li, Z. Chen, and J. Fang, "Multi-irs-aided multiuser MIMO in mmWave/THZ communications: A space-orthogonal scheme," *IEEE Trans. Commun.*, vol. 70, no. 12, pp. 8138–8152, 2022.
- [8] J. A. Zhang et al., "An overview of signal processing techniques for joint communication and radar sensing," *IEEE J. Sel. Topics Signal Process.*, vol. 15, no. 6, pp. 1295–1315, Nov. 2021.
- [9] F. Liu et al., "Integrated sensing and communications: Toward dual-functional wireless networks for 6G and beyond," *IEEE J. Sel. Areas Commun.*, vol. 40, no. 6, pp. 1728–1767, Jun. 2022.
- [10] H. Wymeersch and G. Seco-Granados, "Radio localization and sensing—Part I: Fundamentals," *IEEE Commun. Lett.*, vol. 26, no. 12, pp. 2816–2820, Dec. 2022.
- [11] H. Wymeersch and G. Seco-Granados, "Radio localization and sensing—Part II: State-of-the-art and challenges," *IEEE Commun. Lett.*, vol. 26, no. 12, pp. 2821–2825, Dec. 2022.
- [12] A. Aubry, A. De Maio, and M. Rosamilia, "Reconfigurable intelligent surfaces for N-LOS radar surveillance," *IEEE Trans. Veh. Technol.*, vol. 70, no. 10, pp. 10735–10749, Oct. 2021.
- [13] S. Buzzi, E. Grossi, M. Lops, and L. Venturino, "Radar target detection aided by reconfigurable intelligent surfaces," *IEEE Signal Process. Lett.*, vol. 28, pp. 1315–1319, 2021.
- [14] S. Buzzi, E. Grossi, M. Lops, and L. Venturino, "Foundations of MIMO radar detection aided by reconfigurable intelligent surfaces," *IEEE Trans. Signal Process.*, vol. 70, pp. 1749–1763, 2022.

- [15] W. Lu, Q. Lin, N. Song, Q. Fang, X. Hua, and B. Deng, "Target detection in intelligent reflecting surface aided distributed MIMO radar systems," *IEEE Sensors Lett.*, vol. 5, no. 3, pp. 1–4, Mar. 2021.
- [16] F. Wang, H. Li, and J. Fang, "Joint active and passive beamforming for IRS-assisted radar," *IEEE Signal Process. Lett.*, vol. 29, pp. 349–353, 2022.
- [17] Z. Esmaeilbeig, A. Eamaz, K. V. Mishra, and M. Soltanalian, "Moving target detection via multi-IRS-aided OFDM radar," in *Proc. IEEE Radar Conf. (RadarConf23)*, 2023, pp. 1–6.
- [18] X. Shao, C. You, W. Ma, X. Chen, and R. Zhang, "Target sensing with intelligent reflecting surface: Architecture and performance," *IEEE J. Sel. Areas Commun.*, vol. 40, no. 7, pp. 2070–2084, Jul. 2022.
- [19] Z. Esmaeilbeig, K. V. Mishra, and M. Soltanalian, "IRS-aided radar: Enhanced target parameter estimation via intelligent reflecting surfaces," in *Proc. IEEE 12th Sensor Array Multichannel Signal Process. Workshop* (SAM), 2022, pp. 286–290.
- [20] M. Hua, G. Chen, K. Meng, S. Ma, C. Yuen, and H. C. So, "3D multi-target localization via intelligent reflecting surface: Protocol and analysis," *IEEE Trans. Wireless Commun.*, vol. 23, no. 11, pp. 16527–16543, Nov. 2024.
- [21] M. Hua, Q. Wu, W. Chen, Z. Fei, H. C. So, and C. Yuen, "Intelligent reflecting surface-assisted localization: Performance analysis and algorithm design," *IEEE Wireless Commun. Lett.*, vol. 13, no. 1, pp. 84–88. Jan. 2024.
- [22] X. Song, J. Xu, F. Liu, T. X. Han, and Y. C. Eldar, "Intelligent reflecting surface enabled sensing: Cramér-Rao bound optimization," *IEEE Trans. Signal Process.*, vol. 71, pp. 2011–2026, 2023.
- [23] Z. Yu, X. Hu, C. Liu, M. Peng, and C. Zhong, "Location sensing and beamforming design for IRS-enabled multi-user ISAC systems," *IEEE Trans. Signal Process.*, vol. 70, pp. 5178–5193, 2022.
- [24] C. Liao, F. Wang, and V. K. N. Lau, "Optimized design for IRS-assisted integrated sensing and communication systems in clutter environments," *IEEE Trans. Commun.*, vol. 71, no. 8, pp. 4721–4734, Aug. 2023.
- [25] E. Shtaiwi, H. Zhang, A. Abdelhadi, A. L. Swindlehurst, Z. Han, and H. V. Poor, "Sum-rate maximization for RIS-assisted integrated sensing and communication systems with manifold optimization," *IEEE Trans. Commun.*, vol. 71, no. 8, pp. 4909–4923, Aug. 2023.
- [26] X. Shao, C. You, and R. Zhang, "Intelligent reflecting surface aided wireless sensing: Applications and design issues," *IEEE Wireless Commun.*, vol. 31, no. 3, pp. 383–389, Jun. 2024.
- [27] G. Franken, H. Nikookar, and P. V. Genderen, "Doppler tolerance of OFDM-coded radar signals," in *Proc. Eur. Radar Conf.*, 2006, pp. 108–111.
- [28] C. Sturm, E. Pancera, T. Zwick, and W. Wiesbeck, "A novel approach to OFDM radar processing," in *Proc. IEEE Radar Conf.*, 2009, pp. 1–4.
- [29] C. R. Berger, B. Demissie, J. Heckenbach, P. Willett, and S. Zhou, "Signal processing for passive radar using OFDM waveforms," IEEE J. Sel. Topics Signal Process., vol. 4, no. 1, pp. 226–238, Feb. 2010.
- [30] S. Sen, G. Tang, and A. Nehorai, "Multiobjective optimization of OFDM radar waveform for target detection," *IEEE Trans. Signal Process.*, vol. 59, no. 2, pp. 639–652, Feb. 2011.
- [31] L. Zheng and X. Wang, "Super-resolution delay-doppler estimation for OFDM passive radar," *IEEE Trans. Signal Process.*, vol. 65, no. 9, pp. 2197–2210, May 2017.
- [32] M. F. Keskin, V. Koivunen, and H. Wymeersch, "Limited feedforward waveform design for OFDM dual-functional radar-communications," *IEEE Trans. Signal Process.*, vol. 69, pp. 2955–2970, 2021.
- [33] J. Johnston, L. Venturino, E. Grossi, M. Lops, and X. Wang, "MIMO OFDM dual-function radar-communication under error rate and beampattern constraints," *IEEE J. Sel. Areas Commun.*, vol. 40, no. 6, pp. 1951–1964, Jun. 2022.
- [34] Q. Shi, L. Liu, S. Zhang, and S. Cui, "Device-free sensing in OFDM cellular network," *IEEE J. Sel. Areas in Commun.*, vol. 40, no. 6, pp. 1838–1853, Jun. 2022.
- [35] Y. He, G. Yu, Z. Tang, J. Wang, and H. Luo, "A dual-functional sensing-communication waveform design based on OFDM," *IEEE Trans. Wireless Commun.*, vol. 23, no. 11, pp. 16962–16975, Nov. 2024.

- [36] R. A. Harshman, "Determination and proof of minimum uniqueness conditions for parafac1," *UCLA Work. Papers Phonetics*, vol. 22, no. 111–117, p. 3, 1972.
- [37] J. B. Kruskal, "Three-way arrays: Rank and uniqueness of trilinear decompositions, with application to arithmetic complexity and statistics," *Linear algebra Appl.*, vol. 18, no. 2, pp. 95–138, 1977.
- [38] A. Stegeman and N. D. Sidiropoulos, "On Kruskal's uniqueness condition for the candecomp/parafac decomposition," *Linear Algebra Appl.*, vol. 420, nos. 2–3, pp. 540–552, 2007.
- [39] M. Sørensen and L. De Lathauwer, "Blind signal separation via tensor decomposition with vandermonde factor: Canonical polyadic decomposition," *IEEE Trans. Signal Process.*, vol. 61, no. 22, pp. 5507–5519, Nov. 2013.
- [40] Y. Lin, S. Jin, M. Matthaiou, and X. You, "Tensor-based channel estimation for millimeter wave MIMO-OFDM with dual-wideband effects," *IEEE Trans. Commun.*, vol. 68, no. 7, pp. 4218–4232, Jul. 2020.
- [41] Z. Zhou, J. Fang, L. Yang, H. Li, Z. Chen, and R. S. Blum, "Low-rank tensor decomposition-aided channel estimation for millimeter wave MIMO-OFDM systems," *IEEE J. Sel. Areas Commun.*, vol. 35, no. 7, pp. 1524–1538, Jul. 2017.
- [42] P. Wang, W. Mei, J. Fang, and R. Zhang, "Target-mounted intelligent reflecting surface for joint location and orientation estimation," *IEEE J. Sel. Areas Commun.*, vol. 41, no. 12, pp. 3768–3782, Dec. 2023.
- [43] M. R. Akdeniz et al., "Millimeter wave channel modeling and cellular capacity evaluation," *IEEE J. Sel. Areas in Commun.*, vol. 32, no. 6, pp. 1164–1179, Jun. 2014.
- [44] S. Sun, T. S. Rappaport, M. Shafi, P. Tang, J. Zhang, and P. J. Smith, "Propagation models and performance evaluation for 5g millimeterwave bands," *IEEE Trans. Veh. Technol.*, vol. 67, no. 9, pp. 8422–8439, Sep. 2018.
- [45] G. Zhou, C. Pan, H. Ren, K. Wang, and A. Nallanathan, "A framework of robust transmission design for IRS-aided MISO communications with imperfect cascaded channels," *IEEE Trans. Signal Process.*, vol. 68, pp. 5092–5106, 2020.
- [46] Y. Zhang et al., "Robust transceiver design for covert integrated sensing and communications with imperfect CSI," *IEEE Trans. Commun.*, pp. 1– 1, 2024, doi: 10.1109/TCOMM.2024.3387869.
- [47] E. Ben-Dor, T. S. Rappaport, Y. Qiao, and S. J. Lauffenburger, "Millimeter-wave 60 GHz outdoor and vehicle AOA propagation measurements using a broadband channel sounder," in *Proc. IEEE Global Telecommun. Conf. (GLOBECOM)*, 2011, pp. 1–6.
- [48] Z. Gao, L. Dai, D. Mi, Z. Wang, M. A. Imran, and M. Z. Shakir, "MmWave massive-MIMO-based wireless backhaul for the 5g ultradense network," *IEEE Wireless Commun.*, vol. 22, no. 5, pp. 13–21, Oct. 2015.
- [49] M. Lübke et al., "Validation and analysis of the propagation channel at 60 GHz for vehicular communication," in *Proc. IEEE 94th Vehicular Technol. Conf. (VTC)*, 2021, pp. 1–7.



Jilin Wang (Graduate Student Member, IEEE) received the B.Eng. degree from Tiangong University, Tianjin, China, in 2019. He is currently working toward the Ph.D. degree with the National Key Laboratory of Wireless Communications, University of Electronic Science and Technology of China, Chengdu, China. His research interests include millimeter wave communications, signal processing, and integrated sensing and communications (ISAC).



Jun Fang (Senior Member, IEEE) received the B.S. and M.S. degrees from Xidian University, Xi'an, China, in 1998 and 2001, respectively, and the Ph.D. degree from the National University of Singapore, Singapore, in 2006, all in electrical engineering. In 2006, he was a Postdoctoral Research Associate with the Department of Electrical and Computer Engineering, Duke University. From 2007 to 2010, he was a Research Associate with the Department of Electrical and Computer Engineering, Stevens Institute of Technology. Since 2011, he has been

with the University of Electronic of Science and Technology of China, where he is currently a Professor. His research interests include compressed sensing and sparse theory, massive MIMO/mmWave communications, and statistical inference. He was the recipient of the IEEE Jack Neubauer Memorial Award in 2013 for the best systems paper published in IEEE TRANSACTIONS ON VEHICULAR TECHNOLOGY. He served as an Associate Technical Editor for IEEE Communications Magazine from 2012 to 2020, and a Senior Associate Editor for IEEE SIGNAL PROCESSING LETTERS from 2018 to 2022. He is currently a member of the IEEE SPS Sensor Array and Multichannel TC.



Hongbin Li (Fellow, IEEE) received the B.S. and M.S. degrees from the University of Electronic Science and Technology of China, in 1991 and 1994, respectively, and the Ph.D. degree from the University of Florida, Gainesville, FL, in 1999, all in electrical engineering. From 1996 to 1999, he was a Research Assistant with the Department of Electrical and Computer Engineering, University of Florida. Since 1999, he has been with the Department of Electrical and Computer Engineering, Stevens Institute of Technology, Hoboken, NJ,

where he is currently the Charles and Rosanna Batchelor Memorial Chair Professor. He was a Summer Visiting Faculty Member with the Air Force Research Laboratory, in 2003, 2004, and 2009. His general research interests include statistical signal processing, wireless communications, and radars. He received a number of awards including the IEEE Jack Neubauer Memorial Award in 2013, Master of Engineering (Honoris Causa) from Stevens Institute of Technology in 2024, Provost's Award for Research Excellence in 2019, Harvey N. Davis Teaching Award in 2003, and Jess H. Davis Memorial Research Award in 2001, and Sigma Xi Graduate Research Award in 1999. He has been a member of the IEEE SPS Signal Processing Theory and

Methods Technical Committee (TC) and the IEEE SPS Sensor Array and Multichannel TC, an Associate Editor for *Signal Processing* (Elsevier), IEEE TRANSACTIONS ON SIGNAL PROCESSING, IEEE SIGNAL PROCESSING LETTERS, and IEEE TRANSACTIONS ON WIRELESS COMMUNICATIONS, as well as a Guest Editor for IEEE JOURNAL OF SELECTED TOPICS IN SIGNAL PROCESSING and *EURASIP Journal on Applied Signal Processing*. He has been involved in various conference organization activities, including serving as a General Co-Chair for the 7th IEEE Sensor Array and Multichannel Signal Processing (SAM) Workshop, Hoboken, NJ, 2012. He is a member of Tau Beta Pi and Phi Kappa Phi, and a fellow of the Asia-Pacific Artificial Intelligence Association (AAIA) and the International Artificial Intelligence Industry Alliance (AIIA).



Lei Huang (Senior Member, IEEE) received the B.Sc. and Ph.D. degrees in electronic engineering from Xidian University, Xi'an, China, in 2000 and 2005, respectively. Currently, he is the Chair Professor and Executive Dean of the College of Electronic and Information Engineering, as well as the Executive Director of the State Key Laboratory of Radio Frequency Heterogeneous Integration, Shenzhen University. His research interests include spectral estimation, array signal processing, statistical signal processing, and their applications in radar,

navigation and wireless communications. In these areas, he has published 130 IEEE journal papers, and undertaken 20 national and provincial key projects. He served as a Senior Area Editor of IEEE TRANSACTIONS ON SIGNAL PROCESSING (2019–2023), and an Associate Editor of IEEE TRANSACTIONS ON SIGNAL PROCESSING (2015–2019). He was also on the editorial boards of Elsevier-Digital Signal Processing (2012–2019) and has been on the editorial boards of IET Signal Processing (2017–present), and an Elected Member of Sensor Array and Multichannel (SAM) Technical Committee of the IEEE Signal Processing Society (2016–2022).